

# Performance of Reservoir Discretizations in Quantum Transport Simulations

Justin E. Elenewski,<sup>1,2</sup> Gabriela Wójtowicz,<sup>3</sup> Marek M. Rams,<sup>3,\*</sup> and Michael Zwolak<sup>1,†</sup>

<sup>1</sup>*Biophysical and Biomedical Measurement Group,  
Microsystems and Nanotechnology Division, Physical Measurement Laboratory,  
National Institute of Standards and Technology, Gaithersburg, MD, USA*

<sup>2</sup>*Institute for Research in Electronics and Applied Physics,  
University of Maryland, College Park, MD, USA*

<sup>3</sup>*Jagiellonian University, Institute of Theoretical Physics, Lojasiewicza 11, 30-348 Kraków, Poland*

Quantum transport simulations often use explicit, yet finite, electronic reservoirs. These should converge to the correct continuum limit, albeit with a trade-off between discretization and computational cost. Here, we study this interplay for extended reservoir simulations, where relaxation maintains a bias or temperature drop across the system. Our analysis begins in the non-interacting limit, where we parameterize different discretizations to compare them on an even footing. For many-body systems, we develop a method to estimate the relaxation that best approximates the continuum by controlling virtual transitions in Kramers' turnover for the current. While some discretizations are more efficient for calculating currents, there is little benefit with regard to the overall state of the system. Any gains become marginal for many-body, tensor network simulations, where the relative performance of discretizations varies when sweeping other numerical controls. These results indicate that typical reservoir discretizations have little impact on numerical costs for certain computational tools. The choice of a relaxation parameter is nonetheless crucial, and the method we develop provides a reliable estimate of the optimal relaxation for finite reservoirs.

## I. INTRODUCTION

The design of new electronic materials and nanoelectronic devices requires scalable, high-fidelity approaches to simulate transport. Modern methods can accurately describe the atomic and band structure of many materials, often using density functional theory [1–3]. Moreover, dedicated many-body techniques, such as quantum Monte Carlo or tensor networks, can include contributions from explicit correlations [4–11]. The computational cost of these tools is nonetheless appreciable for large systems or long simulation timescales. These limitations are particularly onerous for tensor networks, where an explicit treatment of the reservoirs will introduce many degrees of freedom [7–15].

A typical transport simulation is shown in Fig. 1, where a system (device) of interest is coupled to explicit reservoirs. Transport is maintained by a bias. In a closed system, this could be introduced by a density imbalance or a time-dependent, inhomogeneous on-site potential in the reservoirs. Open systems can go a step further by including implicit reservoirs, which drive transport by relaxing explicit reservoir modes to biased Fermi distributions [16–22]. The *extended reservoir approach* exemplifies such an arrangement, and it has become popular in many guises [16–39], including those that accommodate many-body transport [8–11].

These computational methods employ reservoirs that are discretized. While a given discretization should converge to the spectral function of a continuum reservoir, its construction is otherwise arbitrary. This flexibility

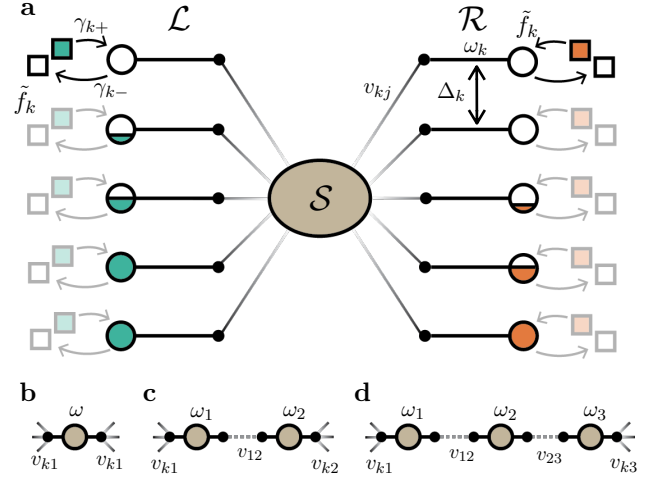


FIG. 1. **Quantum transport with extended reservoirs.** (a) An arbitrary impurity ( $S$ ) is flanked by explicit left ( $\mathcal{L}$ ) and right ( $\mathcal{R}$ ) reservoirs. Each reservoir contains  $N_W$  modes of frequencies  $\omega_k$  that couple to a designated system site  $i$  with constant strength  $v_{ki}$ . Implicit reservoirs relax  $\mathcal{L}$  and  $\mathcal{R}$  to biased Fermi distributions  $\tilde{f}_k$  at a rate  $\gamma_k$  for the  $k^{\text{th}}$  mode. We consider models for  $S$  that include (b) one, (c) two, and (d) three site systems with onsite frequencies  $\omega_i$ . These sites couple to each other with strength  $v_{ij}$  and to the reservoirs at terminal sites (i.e., a single system mode couples to each reservoir).

has resulted in a variety of approaches, including the placement of modes evenly across the bandwidth (linear discretization), assigning them according to the canonical transform of finite tight-binding lattices, distributing them evenly inside the bias window and logarithmically outside (linear-logarithmic) [10, 14, 40, 41], and using an

\* marek.rams@uj.edu.pl

† mpz@nist.gov

influence-based approach that yields linear mode spacing across the bias window and an inverse spacing outside (linear-inverse) [42]. Moreover, the deviation of finite representations from the continuum can be corrected for perturbatively [43, 44]. Related techniques aim to minimize the number of reservoir modes by introducing *intermode* transitions during relaxation. While these additional fitting parameters provide a higher fidelity spectral density [12, 13, 15, 45], they also add numerous long-range couplings from the intermode relaxations. This ultimately limits the feasible size of reservoirs. Ideally, one desires high accuracy simulations at low computational cost (and favorable scaling). It is unclear what approach performs best, as a quantitative comparison does not exist.

Here, we address one very important facet of this comparison: How does the choice of reservoir discretization influence the computational cost needed to converge transport properties to a given accuracy? We also examine how the system-reservoir coupling and implicit relaxation impact the convergence of steady-state transport. We study non-interacting systems and their many-body counterparts, but only consider extended reservoirs with *intramode* Markovian relaxation [8, 16–22]. For non-interacting systems, we optimize the relaxation (e.g., discretization and coupling to implicit modes) to get the highest accuracy in steady-state currents. This procedure has limited generality since it requires knowledge of the exact, continuum reservoir solution. For the many-body case, we demonstrate how Kramers' turnover can be used to estimate an optimal relaxation rate.

We find that certain discretizations can increase efficiency for non-interacting calculations, where efficiency is measured by the number of reservoir modes required to reproduce the current up to a fixed accuracy. This advantage is weak for other system observables (e.g., the impurity's density) and its correlation matrix, particularly when working at small to moderate reservoir sizes. While tensor network calculations exhibit moderate, discretization-dependent deviations in the impurity correlation matrix, we find that the overall efficiency is tied to other control parameters — most importantly, the Schmidt cutoff. This behavior reflects the natural structure of our tensor network, which uses an energy/momentum basis for the explicit reservoirs and orders them globally according to their energies to minimize the bipartite entanglement in the numerical ansatz. While certain discretizations reduce the number of modes, they do so for energy scales that are weakly correlated. These scales contribute little to the computational cost. Thus, the choice of discretization has little practical impact on efficiency.

## II. BACKGROUND AND SETUP

We follow a conventional arrangement [46, 47] that consists of non-interacting left ( $\mathcal{L}$ ) and right ( $\mathcal{R}$ ) reser-

voirs, and a bias that drives transport through a impurity system ( $\mathcal{S}$ ), see Fig. 1. The associated Hamiltonian has the form  $H = H_{\mathcal{S}} + H_{\mathcal{L}} + H_{\mathcal{R}} + H_{\mathcal{I}}$ , where  $H_{\mathcal{S}}$  is the (potentially many-body) Hamiltonian for  $\mathcal{S}$ ,  $H_{\mathcal{L}(\mathcal{R})} = \sum_{k \in \mathcal{L}(\mathcal{R})} \hbar \omega_k c_k^\dagger c_k$  are the reservoir Hamiltonians, and  $H_{\mathcal{I}} = \sum_{k \in \mathcal{L}\mathcal{R}} \sum_{i \in \mathcal{S}} \hbar (v_{ki} c_k^\dagger c_i + v_{ik} c_i^\dagger c_k)$  is the interaction Hamiltonian that couples  $\mathcal{S}$  to  $\mathcal{L}\mathcal{R}$ . The  $c_m^\dagger$  ( $c_m$ ) are fermionic creation (annihilation) operators for a state  $m \in \mathcal{L}\mathcal{S}\mathcal{R}$ . All indices implicitly include multiple relevant labels (such as mode number, reservoir, and spin). The frequency for the  $k^{\text{th}}$  reservoir mode is denoted by  $\omega_k$ , while  $v_{ki} = v_{ik}^*$  is used for the coupling between  $i \in \mathcal{S}$  and  $k \in \mathcal{L}\mathcal{R}$ . For two-site impurity  $\mathcal{S}$ , the Hamiltonian is

$$H_{\mathcal{S}} = \hbar v_{\mathcal{S}} (c_1^\dagger c_2 + c_2^\dagger c_1) + \hbar U n_1 n_2, \quad (1)$$

where  $v_{\mathcal{S}}$  is the internal coupling in  $\mathcal{S}$ ,  $n_i = c_i^\dagger c_i$  is the particle number operator for site  $i$ , and  $U$  is the many-body density-density interaction strength [8]. The description of other models can be found in the Supplemental Information (SI). This model corresponds to a (time-independent) photoconductive molecular device where spin can be neglected [48].

We calculate the properties of non-interacting systems, including the impurity's correlation matrix, using non-equilibrium Green's functions [16–18, 20, 21], and employ tensor networks for the many-body case [8, 22]. When considering the latter, we solve a Lindblad master equation

$$\begin{aligned} \dot{\rho} = & -\frac{\gamma}{\hbar} [H, \rho] + \sum_{k \in \mathcal{L}\mathcal{R}} \gamma_{k+} \left( c_k^\dagger \rho c_k - \frac{1}{2} \{c_k c_k^\dagger, \rho\} \right) \\ & + \sum_{k \in \mathcal{L}\mathcal{R}} \gamma_{k-} \left( c_k \rho c_k^\dagger - \frac{1}{2} \{c_k^\dagger c_k, \rho\} \right), \quad (2) \end{aligned}$$

for the  $\mathcal{L}\mathcal{S}\mathcal{R}$  system with Markovian relaxation in  $\mathcal{L}\mathcal{R}$  (here  $\{\cdot, \cdot\}$  is the anticommutator). The first term gives evolution of the many-body density matrix  $\rho$  under our Hamiltonian  $H$ , while the second and third terms give open dynamics through injection and depletion of the modes  $k$  at rates  $\gamma_{k+}$  and  $\gamma_{k-}$ , respectively. To ensure that the reservoirs relax to the fully isolated  $\mathcal{L}\mathcal{R}$  state, we set these rates to  $\gamma_{k+} \equiv \gamma_k f^\alpha(\omega_k)$  and  $\gamma_{k-} \equiv \gamma_k [1 - f^\alpha(\omega_k)]$ , where  $f^\alpha(\omega_k)$  is the Fermi-Dirac distribution in the  $\alpha \in \{\mathcal{L}, \mathcal{R}\}$  reservoir.

We quantify accuracy of the steady-state current  $I$  for non-interacting models using a relative error  $|I - I^\circ|/I^\circ$ , where the reference current  $I^\circ$  is the Landauer limit for continuum reservoirs [49] (we work with the current itself for many-body cases, as  $I^\circ$  is not known exactly). Furthermore, we quantify combined error in occupancy and correlations using the correlation matrix of  $\mathcal{S}$ , i.e.  $\mathcal{C}_{\mathcal{S}} = \mathcal{C}_{ij} = \langle c_i^\dagger c_j \rangle$ , with  $i, j \in \mathcal{S}$ . The quantity  $\mathcal{C}_{\mathcal{S}}$  completely characterizes all equal time correlations for non-interacting systems, and includes the information on densities (occupancy)  $n_i = \mathcal{C}_{ii}$ . A natural metric for convergence of the system state is the normalized trace

distance,  $\|C_S - C_S^{\circ}\|_* = \|C_S - C_S^{\circ}\|/2[\text{tr} C_S + \text{tr} C_S^{\circ}]$ , defined in terms of the trace norm  $\|M\| = \text{tr}\sqrt{M^\dagger M}$  and the exact correlation matrix  $C_S^{\circ}$  for continuum reservoirs.

Discretizations are compared by maintaining a common set of modes within the bias window  $\mathcal{B}$ , while distributing modes outside the bias window  $\mathcal{W} \setminus \mathcal{B}$  according to a designated arrangement (here  $\mathcal{W}$  denotes both the reservoir band and its bandwidth). We formalize this by associating an abstract influence scale  $\chi(\omega)$  with each discretization, which we use to specify mode placement within the reservoir bandwidth. In this manner, the functional form of  $\chi(\omega)$  completely specifies a given discretization. Mode placement begins by defining integrated weights for modes inside  $X_{\mathcal{B}} = \int_{\mathcal{B}} \chi(\omega) d\omega$  and outside  $X_{\mathcal{W} \setminus \mathcal{B}} = \int_{\mathcal{W} \setminus \mathcal{B}} \chi(\omega) d\omega$  the bias window. We also introduce an integrated influence per mode  $x$  (a target weight per mode) that specifies  $N_{\mathcal{B}} = \lceil X_{\mathcal{B}}/x \rceil$  modes in the bias window and  $N_{\mathcal{W} \setminus \mathcal{B}} = \lceil X_{\mathcal{W} \setminus \mathcal{B}}/x \rceil$  outside the bias window. The region  $\mathcal{B}$  is then divided into  $N_{\mathcal{B}}$  bins  $\Delta_k$  with boundaries satisfying  $\int_{\Delta_k} \chi(\omega) d\omega = X_{\mathcal{B}}/N_{\mathcal{B}}$  and  $\cup_{k \in \mathcal{B}} \Delta_k = \mathcal{B}$  (similarly for the complement of  $\mathcal{B}$ ). We choose values of  $x$  so that there is always an even number of symmetrically distributed modes in both  $\mathcal{B}$  and  $\mathcal{W} \setminus \mathcal{B}$ . This accommodation ensures that there is never a mode at the Fermi level. Reservoir modes are then placed at the midpoint  $\omega_k$  of each bin.

We compare three reservoir discretizations: (i) a linear case, with modes spaced evenly throughout the bandwidth; (ii) a linear–logarithmic discretization (motivated by energy scale separation under the numerical renormalization group [50]); and (iii) a linear–inverse arrangement following the influence approach of Ref. [42]. The influence scales for these discretizations are

$$\chi_{\text{lin}}(\omega) = 1 \quad (3)$$

$$\chi_{\text{log}}(\omega) = \theta\left(\frac{\mu}{2} - |\omega|\right) + \frac{\mu}{2|\omega|} \theta\left(|\omega| - \frac{\mu}{2}\right) \quad (4)$$

$$\chi_{\text{inv}}(\omega) = \theta\left(\frac{\mu}{2} - |\omega|\right) + \left(\frac{\mu}{2\omega}\right)^2 \theta\left(|\omega| - \frac{\mu}{2}\right), \quad (5)$$

which are nonzero within the reservoir bandwidth and zero outside, as depicted in Fig. 2a. Here,  $\theta(x)$  is the Heaviside step function. All three measures give evenly spaced modes within  $\mathcal{B}$  yet differ in  $\mathcal{W} \setminus \mathcal{B}$ , acknowledging that bias window modes contribute significantly to the current. Our terminology reflects a measure of influence that is given by the integral of  $\chi$ .

Using these, we compare simulations with the reservoir relaxation rate  $\gamma_k$  a fixed multiple of the mean level spacing in the bias window  $\langle \Delta_k \rangle_{\mathcal{B}}$  (this is equal to  $\mu/N_{\mathcal{B}}$  for all cases herein) to the relaxation defined by the mode-dependent level spacing  $\Delta_k$ . We also compare system–reservoir couplings that are defined by the midpoint between two discrete reservoir modes to couplings defined by the integrated coupling over an interval of width  $\Delta_k$  about a mode  $\omega_k$  (which is placed at the center of the bin) [51].

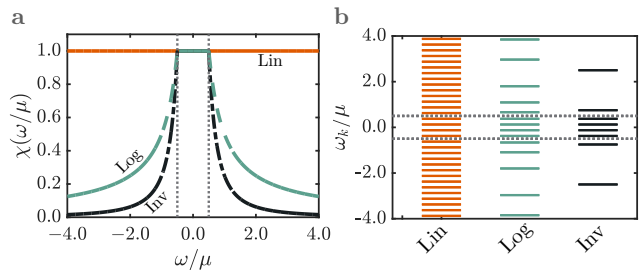


FIG. 2. **Influence scales and discretizations.** (a) influence scales that induce linear ( $\chi_{\text{lin}}(\omega)$ ; orange, solid), linear–logarithmic ( $\chi_{\text{log}}(\omega)$ ; green, dashed), and linear–inverse ( $\chi_{\text{inv}}(\omega)$ ; black, dash-dot) discretizations. (b) The resulting minimal mode distributions  $\omega_k$ , calculated at the same integrated influence per mode  $x$ . Thin dotted lines in both plots demarcate the bias window edge. Data are at a bias  $\mu = \omega_0/2$  and reservoir bandwidth  $\mathcal{W} = 4\omega_0$ , where  $\omega_0$  is the real–space hopping in the reservoir. Modes near the band edges of the linear–logarithmic discretization are a consequence of the chosen influence scale, bias, and bandwidth — they are not necessarily present for denser distributions.

### III. KRAMERS' TURNOVER

The composite  $\mathcal{LSR}$  system exhibits distinct transport regimes in the presence of relaxation [16] which mimic Kramers' turnover for chemical reaction rates, see Fig. 3a [52] (a similar result holds for thermal transport [53–57]). When relaxation is weak, transport is determined by the rate at which particles and holes are replenished in the extended reservoirs. In this regime the current will rise proportionally with the mode–dependent relaxation rate  $\gamma_k$ , analogous to chemical systems where environmental friction controls the equilibration of reacting species. When the relaxation is strong, phase coherence is suppressed and the current decays as  $\gamma_k^{-1}$ . Here, transport emulates reactions where strong friction redirects partially formed products back to the reactants (i.e., recrossings). The intermediate region contains a plateau–like region where the continuum limit current is reproduced, analogous to reactions that are controlled by the transition state rate. As we will emphasize later, the system state does not necessarily reflect the exact model on the whole plateau. The width of the plateau—and convergence to this limit—is dominated by the number and distribution of explicit reservoir modes. The natural transport rate only predominates in the intermediate region [16].

The formation of the plateau as  $N_{\mathcal{W}} \rightarrow \infty$  and  $\gamma_k \rightarrow 0$  (in that order) is sufficient to determine the continuum current, though not all points on the plateau will correspond to a fully converged system state (e.g., local electronic densities). Moreover, this regime is not guaranteed to be unambiguous. There may be additional features due to the underlying Hamiltonian [8, 18] or the presence of specific *anomalies* which exist on either side of the

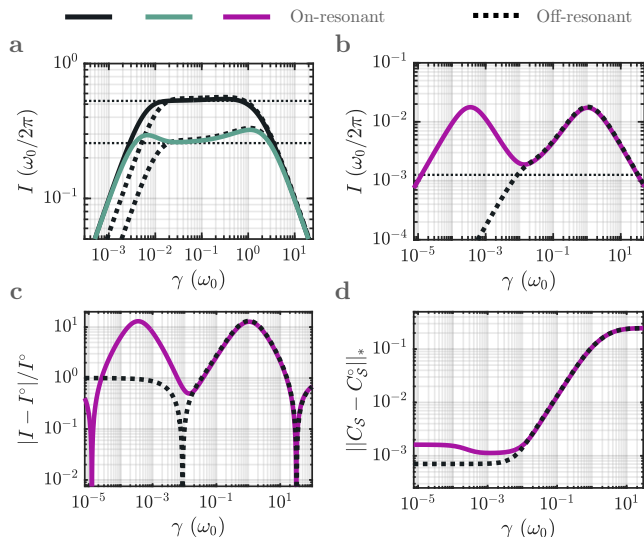


FIG. 3. **Kramers' turnover and accuracy.** Steady-state transport for a two-site model and discrete reservoirs with mode-independent reservoir relaxation  $\gamma_k = \gamma$ . Data are presented for on-resonant reservoir modes (solid lines) and those made off-resonant via a frequency shift  $\langle \Delta_k \rangle_B/2$  between isoenergetic modes (dotted lines). (a) Current turnover  $I(\gamma)$  at strong system-reservoir coupling  $v_0 = \omega_0/2$  and for two system-site couplings,  $v_S = (1 + \sqrt{2})\omega_0/4$  (black) and  $v_S = (2 + \sqrt{3})\omega_0/4$  (green), showing different plateau topographies at different intrasite coupling scales. (b) Current turnover at small system-reservoir coupling,  $v_0 = \omega_0/10$ , reveal anomalies on either side of an interstitial Landauer regime ( $v_S = (1 + \sqrt{2})\omega_0/4$ ) [22]. (c) Relative current error with respect to the continuum limit  $I^\circ$  for the model in (b). (d) Convergence of the system state via the normalized trace distance between finite  $C_S$  and continuum  $C_S^\circ$  correlation matrices, illustrating that no conditions are uniformly optimal for all observables (the current impacts this convergence in limited manner; see the SI). The continuum (Landauer) limit is denoted by the dotted horizontal line. All calculations use  $N_W = 128$  explicit reservoir modes, spaced evenly between  $\pm W/2$  and integrated couplings (see Ref. [49]). We apply a symmetric bias  $\mu = \omega_0/2$  between reservoirs both held at temperature  $T = \omega_0/40$ .

plateau (Fig. 3a,b) [22]. For large relaxation, a *Markovian anomaly* is associated with an unphysical broadening of reservoir modes and the lack of a well-defined Fermi level [16]. This is a direct consequence of Markovian relaxation, which fills a reservoir mode according to its bare frequency  $\omega_k$  rather than accounting for its broadening. Such behavior can lead to zero bias currents in some cases [16]. These concerns are irrelevant for non-Markovian relaxation, where reservoir modes are properly occupied according their broadened density of states.

For weak relaxation, a *virtual anomaly* occurs due to virtual transitions through the system, specifically between on-resonant  $\mathcal{L}$  and  $\mathcal{R}$  modes. This leads to excess transport, as previously seen in Refs. [8, 38] and

explained in Ref. [22]. The virtual anomaly can be suppressed by shifting the relative energy of  $\mathcal{L}$  and  $\mathcal{R}$  by half the level spacing,  $\Delta_k/2$ , disrupting the resonant structure. While anomalous regimes can be difficult to distinguish at strong system-reservoir coupling (e.g.,  $v_0 \approx \omega_0/2$ ), they become prominent when the coupling is weak (e.g.,  $v_0 \approx \omega_0/10$ ), see Fig. 3b.

Various factors, including the finite distribution of reservoir modes and the specific Hamiltonian, can influence the turnover architecture (e.g., weak and strong coupling can have a different optimal relaxation as a function of  $N_r$  [22]). Thus, we need a method that compares discretizations while not placing any given discretization at a disadvantage *a priori*. We obtain this for non-interacting systems by choosing a relaxation that most accurately reflects the steady-state current of continuum reservoirs. For many-body cases, we estimate the optimal relaxation as described later in the manuscript.

#### IV. OPTIMAL RELAXATION

We can obtain the exact, continuum-limit current of non-interacting systems using established methods. For finite reservoirs, there is an optimal relaxation located in the intermediate, physical turnover regime that best estimates this current (see Fig. 3; we exclude incidental crossovers at weak and strong relaxation). To proceed, we must quantify this optimum for reservoirs with an inhomogeneous mode spacing. We begin by introducing a relaxation  $\gamma_k = \alpha \eta(\omega_k)$ , where  $\alpha > 0$  is a real scaling constant and  $\eta(\omega_k)$  is a function of the level spacing within the extended reservoirs. Using this convention, we examine  $\eta(\omega_k)$  as either (i) a constant independent of  $k$  (in some cases, we set this constant to the average bias window level spacing) or (ii) to the  $k$ -dependent level spacing. We then seek an  $\alpha^*$  in the intermediate region that minimizes the relative current error  $\alpha^* = \arg \min(|I[\gamma_k(\alpha)] - I^\circ|/I^\circ)$  with respect to the continuum limit  $I^\circ$ . This  $\alpha^*$  completely defines the optimal relaxation for both equally and unequally spaced cases (with a single  $\gamma^* = \gamma_k$  for equally spaced modes). In some cases we could also derive an optimal relaxation using the normalized trace distance between correlation matrices (see Fig. 3d) though we do not take this approach. Convergence of this quantity would ensure convergence of all other (time-local) system observables [58], including the current if there is a boundary that divides the impurity into left and right parts. This relaxation would not necessarily coincide with  $\gamma^*$  as defined above [59].

When the exact, continuum limit current  $I^\circ$  is unknown, as is the case for most interacting systems, there is no obvious way to optimize  $I[\gamma_k(\alpha)]$ . This point is critical in practical calculations. Optimization can also fail when the plateau is featureless (e.g., at strong-coupling in Fig. 3a), when many plateau features are present [18], or if convergence occurs from below the Landauer limit (see the SI). We can, however, estimate an optimal regime

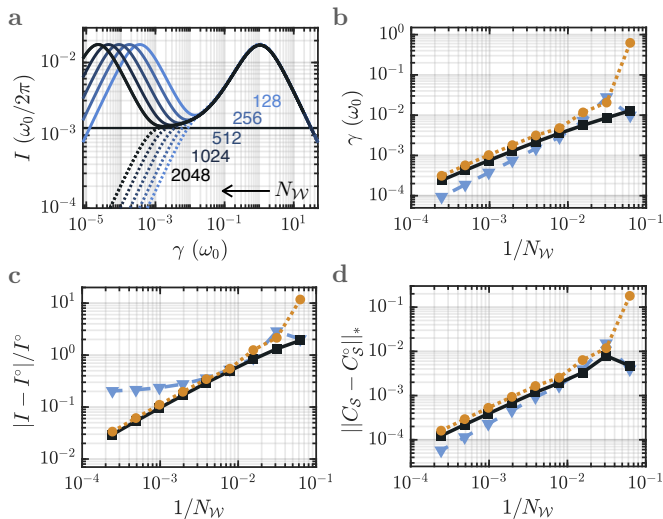


FIG. 4. **Optimal relaxation and estimators.** (a) Elongation of the region between anomalies as the number of reservoir modes  $N_W$  is increased. Turnover profiles are shown with (dotted line) and without (solid line) a frequency shift of  $\langle \Delta_k \rangle_B / 2$  between isoenergetic modes in  $\mathcal{L}$  and  $\mathcal{R}$ , defined by the mean level spacing in the bias window. (b) Determination of the best estimator for the Landauer regime  $I[\gamma^*] = I[\gamma_k(\alpha^*)]$  (black diamond). Estimators are based on either  $\gamma_\ell$  (blue circle)—the linear extrapolation of the small- $\gamma$  regime of the shifted model (off-resonant; blue, dashed) into the unshifted (on-resonant) profile—or  $\gamma_s$  (tan circle)—the intersection between shifted and unshifted profiles. Scaling of relaxation associated with  $\gamma_\ell$  and  $\gamma_s$  estimators: (c) Convergence of the relative current error  $|I - I^0|/I^0$  and (d) the trace norm  $\|C_S - C_S^0\|_*$  with respect to  $N_W$ . All scaling profiles correspond to  $\gamma^* = \gamma_k(\alpha^*)$  (black, square), the linear extrapolation estimator (blue, triangle), and the intersection of shifted/unshifted turnover profiles (tan, circle). All panels reflect a linear reservoir discretization for the weak coupling model of Fig. 3b.

by applying a relative shift of  $\langle \Delta_k \rangle_B / 2$  between isoenergetic states in  $\mathcal{L}$  and  $\mathcal{R}$  reservoirs. That is, we shift the modes in  $\mathcal{L}$  and  $\mathcal{R}$  by plus/minus a quarter of the level spacing. As noted earlier, this eliminates the virtual anomaly associated with resonant transitions [22]. The shifted profile should intersect the unshifted profile at a point  $\gamma_s$  near the physical regime  $\gamma^*$  [60]. A second estimate is given by extrapolating the linear, small- $\gamma$  regime of the shifted case and finding the point  $\gamma_\ell$  where this intersects the unshifted profile. This  $\gamma_\ell$  will typically lie prior to  $\gamma^*$ .

Figure 4a shows these two estimators. Since the region between anomalies expands into an almost flat profile with an increasing number of reservoir sites, we expect these estimators to bound  $\gamma^*$  on either side for large  $N_W$ . This is indeed the case here. Moreover, the intersection estimator  $\gamma_s$  tightly reproduces the optimal point  $I[\gamma_k(\alpha^*)]$  starting at moderate  $N_W$ . In contrast, the extrapolation estimator  $\gamma_\ell$  moves away from the optimum

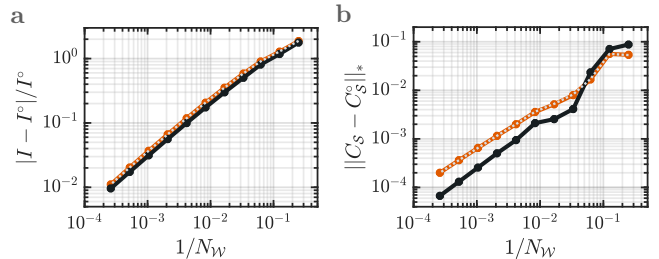


FIG. 5. **Coupling and relaxation methods.** Convergence of the steady-state current  $I[\gamma_k(\alpha^*)]$  using integrated couplings and mode-dependent relaxation. Error in  $I$  is shown for (a) integrated couplings with relaxation defined by the mean bias window spacing  $\gamma_k = \alpha^* \langle \Delta_k \rangle_B$  (black, solid) or by the level spacing  $\gamma_k = \alpha^* \Delta_k$  (orange, dashed), where  $\alpha^*$  is the optimal prefactor. (b) Convergence of the system state, as reflected by the normalized trace distance  $\|C_S - C_S^0\|_*$  between correlation matrices, for the same methods as (a). The grey dotted line in (a) and (b) has  $\gamma_k = \alpha^* \Delta_k$ , but with couplings from the midpoint of the discretization intervals. The model is otherwise that of Fig. 3b with a linear-inverse discretization.

as  $N_W$  increases (see Fig. 4c and the SI). This is a consequence of the plateau topography. That is, the estimator  $\gamma_\ell$  scales with  $1/N_W$  and rides the edge of the virtual anomaly as  $N_W \rightarrow \infty$ . However, there is a duality between virtual and Markovian anomalies, which can make the optimal relaxation scale as  $1/\sqrt{N_W}$  in the moderate  $N_W$  regime [22]. Thus, in this moderate regime, the  $\gamma_\ell$  departs from the optimal relaxation and its error saturates.

The intersection estimator  $\gamma_s$  is also robust when examining the overall state of the system (Fig. 4e). However, the extrapolation estimator  $\gamma_\ell$  actually outperforms both the optimal and intersection estimators for this case (see Fig. 4e and the SI). We consider this incidental as it is due to the fact that smaller relaxation often results in a more accurate system correlation matrix, see Fig. 3d [61]. Despite this, the intersection estimator is better behaved. Thus, to find the Landauer limit, we only need to calculate turnover profiles with on-resonant and off-resonant reservoir modes and find their intersection  $\gamma_s$  — an approach that is borne out for other models and in the strong coupling limit (see the SI). While Hamiltonian parameters can change the plateau architecture, the intersection between turnover profiles will invariably remain a useful estimator of the physical (continuum) regime.

## V. RESULTS

Having established a framework to compare different discretizations, we now examine both non-interacting and many-body transport. As a first step, we compare different system-reservoir coupling methods and different choices of  $\eta(\omega_k)$  for the non-interacting case.

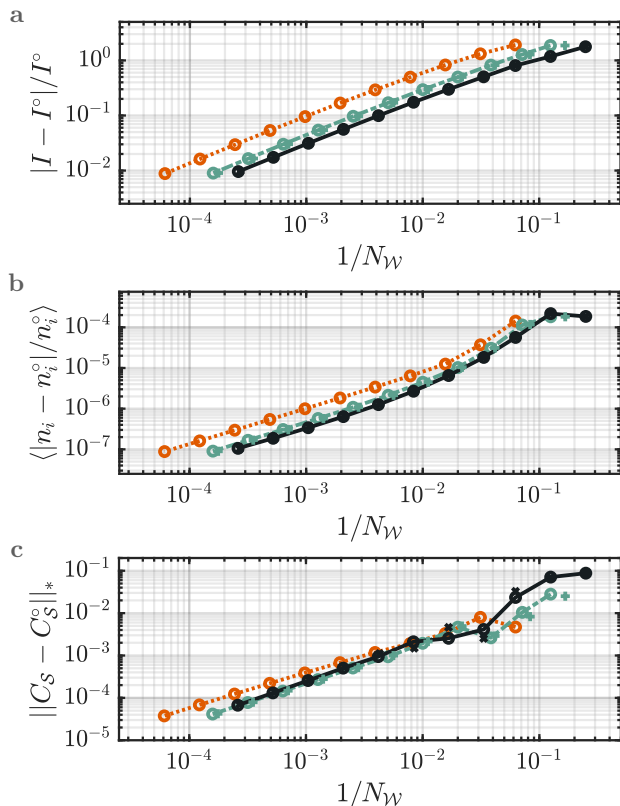


FIG. 6. **Error and discretization.** Convergence of reservoir discretizations when increasing the number  $N_W$  of explicit reservoir sites. This behavior is quantified through (a) relative error in the steady-state current  $I[\gamma_k(\alpha^*)]$ ; (b) the mean relative error of the on-site densities  $n_i$  within  $\mathcal{S}$ ; and (c) the normalized trace distance between correlation matrix  $C_S$  for  $\mathcal{S}$  and its infinite reservoir counterpart  $C_S^0$ . Discretizations correspond to the standard linear (orange, dotted line), the linear-logarithmic (green, dashed line), and the linear-inverse (black, solid line) arrangements. Results are also provided for modified linear-logarithmic and linear-inverse discretizations that incorporate the 1D spectral density into the influence scale (this pinches off the influence at the band edge) (green and black crosses). Profiles from (a) fit to  $A/N_W^p$  with  $[A, p] = [11 \pm 1, -0.65 \pm 0.02]$ ,  $[8.5 \pm 0.2, -0.72 \pm 0.01]$ , and  $[4.4 \pm 0.2, -0.64 \pm 0.18]$  for the main discretizations. All data are from the non-interacting, two-site Hamiltonian of Fig. 3b at weak-coupling ( $v_0 = \omega_0/10$ ), with integrated system-reservoir couplings, and relaxations  $\gamma = \alpha \langle \Delta_k \rangle_{\mathcal{B}}$  determined by the mean mode spacing within the bias window  $\mathcal{B}$ .

### A. Non-interacting systems

The behavior of a reservoir discretization may be influenced by the system-reservoir coupling and the assignment of relaxation rates  $\gamma_k$  to each reservoir mode. We present this behavior for the linear-inverse discretization in Fig. 5. The more significant factor is the choice of relaxation, which nontrivially moderates convergence to the continuum limit with increasing  $N_W$ . The error in  $I$  is smaller when the relaxation is a multiple of the mean

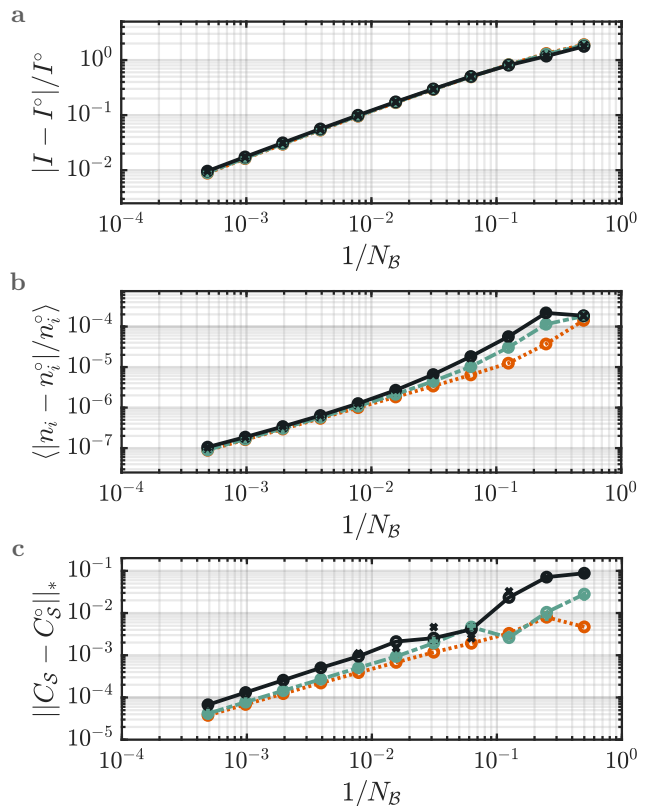


FIG. 7. **Error and discretization in the bias window.** Convergence of the reservoir discretizations from Fig. 6, now parameterized in terms of the number of states  $N_B$  in the bias window. Scaling is quantified through (a) relative error in the steady-state current  $I[\gamma_k(\alpha^*)]$ ; (b) the mean relative error of the on-site densities  $n_i$  within  $\mathcal{S}$ ; and (c) the normalized trace distance between correlation matrix  $C_S$  for  $\mathcal{S}$  and its infinite reservoir counterpart  $C_S^0$ . Colors and symbols follow from Fig. 6. Profiles from (a) fit to  $A/N_B^p$  with  $[A, p] = [4.1 \pm 0.1, -0.76 \pm 0.02]$ ,  $[4.0 \pm 0.2, -0.76 \pm 0.02]$ , and  $[3.8 \pm 0.3, -0.74 \pm 0.03]$  for the main discretizations, while restricting to  $N_B > 4$  to mitigate finite size effects. These results indicate that, for the current, it is the convergence of the spectral density in the bias window that matters. If arbitrary observables are desired, however, the spectral density at higher frequencies is relevant.

level spacing in the bias window,  $\gamma_k = \alpha \langle \Delta_k \rangle_{\mathcal{B}}$  (which, in the cases here, is equal to  $\mu/N_B$ ). This situation is more variable for convergence of  $C_S$ , where we see better performance at small  $N_W$  if the relaxation is a multiple of the level spacing  $\gamma_k = \alpha \Delta_k$  (Fig. 5a,b). Nonetheless, this behavior crosses over to favor the mean-spacing approach at modest  $N_W$ . We note that convergence is minimally impacted by the coupling method — the integrated and mean methods do not differ appreciably at any  $N_W$  scale. From here on, we employ mode-independent relaxation  $\gamma_k = \gamma$  and the integrated coupling constants.

Figure 6 shows the performance of different discretizations when converging a transport calculation. We find

the full linear discretization  $\chi_{\text{lin}}(\omega)$  to behave more poorly in terms of either the relative error in current  $I$  or in the system-site density  $n_i$  (Fig. 6a,b). Notably, the error in the steady-state current is uniformly higher than the other discretizations for all values of  $N_{\mathcal{W}}$ . Using the same criteria, the linear-inverse influence measure  $\chi_{\text{inv}}(\omega)$  outperforms the linear-logarithmic discretization  $\chi_{\text{log}}(\omega)$ . This implies a lower degree of error at fewer reservoir sites, providing better convergence in a regime with decreased computational cost. The performance gain when moving between these methods is nonetheless smaller than the gain when moving to them from the full linear discretization.

Any advantage is less clear-cut for the overall state of the system, where all three discretizations exhibit comparable performance at large  $N_{\mathcal{W}}$ . Nonetheless, the linear-inverse discretization performs more poorly when  $N_{\mathcal{W}}$  is small — a region where convergence can oscillate due to the placement of states outside the bias window edge. Similar conclusions may be drawn for models containing one or three sites (Fig. 1b,d; see SI). These methods are roughly equivalent for the number of states used in typical many-body transport simulations (i.e.,  $N_{\mathcal{W}}$  in the 100's).

A parallel analysis can be done in terms of the number of reservoir modes  $N_{\mathcal{B}}$  within the bias window (Fig. 7). This region is particularly important when representing the current, and the accuracy of a representation correlates with  $N_{\mathcal{B}}$ . Working from this perspective, we find uniform scaling across discretizations with respect to the current error. This observation simply reflects that transport is dominated by bias window modes and one needs to accurately represent the spectral density in that window. The occupations also scale uniformly at large  $N_{\mathcal{B}}$ , albeit with discrepancies when this parameter is small. Correlation matrices have more sporadic behavior, though the linear-inverse arrangement reproduces the system state most poorly at a given  $N_{\mathcal{B}}$ . This reflects a lower fidelity spectral density outside of the bias window. The performance gap for the linear-inverse is nonetheless offset by the overall reduction in  $N_{\mathcal{W}}$  at a given integrated influence per mode, as seen in Fig. 6c.

## B. Many-body impurities

To study complex, interacting models we require sophisticated numerical methods, such as tensor networks. We adopt a typical approach for open quantum systems, where the density matrix is vectorized and approximated as a one-dimensional tensor network, also called a matrix product state (MPS) [63, 64]. While the MPS has a one dimensional structure, this does not require that the Hamiltonian have only local interactions. The MPS may also tolerate long-range couplings, particularly when a judicious state ordering is imposed for the reservoirs (as in our ordering for the mixed basis in Fig. 8). These give a small, fixed MPO dimension. This construction is

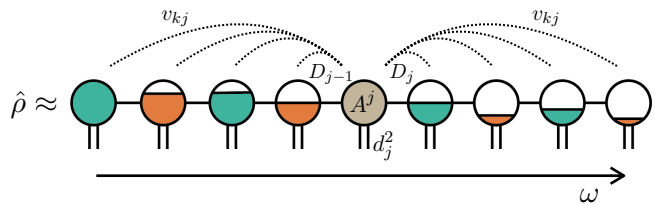


FIG. 8. **Matrix product state ansatz.** The reservoirs (orange/green) are represented in the energy basis (similar to the so-called star geometry [62]), where we mix the modes from the two reservoirs along the one-dimensional MPS lattice, ordering them globally according to their energies and keeping the impurity sites (brown) in the middle. This order reflects the natural scattering structure of the current-carrying states [7, 8], greatly reducing the bipartite entanglement in the lattice and the MPS bond dimension needed to achieve a given level of precision. The color-coding follows Fig. 1.

represented diagrammatically in Fig. 8, where we have ordered the combined  $\mathcal{LR}$  modes (green/orange) according to their energies, reflecting the resonant nature of the current-carrying states [7, 8] (the color-coding follows Fig. 1). The system  $\mathcal{S}$  (grey) is positioned in the middle at  $\omega = 0$ . Following this notation,  $d_j$  is the local Hilbert space dimension at site  $j$  and  $D_j$  is the MPS bond dimension to the right of site  $j$ . The latter determines the size  $D_{j-1} \times d_j^2 \times D_j$  of each tensor  $A^j$  constituting the MPS. The computational cost will depend on both  $N_{\mathcal{W}}$  and the structure of the correlations, which set the minimal  $D_j$  needed to reach a given level of accuracy. Our choice of reservoir mode ordering has been shown to minimize this bond dimension by mitigating the spread of entanglement [7, 8]. We obtain steady-states by using the time-dependent variational principle [65] to evolve an MPS under the Lindblad superoperator, as described in Ref. [8] (see Ref. [9] for a similar approach with a different state ordering). Since the accuracy of this approach depends on the bond dimension, we can adjust the latter using a cutoff  $\epsilon_{\text{min}}$ . That is, we only retain the singular values that are above this cutoff for each bipartition of the lattice in Fig. 8.

We quantify convergence of our MPS calculations via the steady-state current, which is expected to have consistently larger error than other measures. Our analysis will focus on the weakly-coupled, two-site impurity model from Fig. 6 in both non-interacting and interacting limits. To assess the consistency of our methods, we first confirm that the current and correlation matrix from the non-interacting MPS can reproduce the exact solution for all three discretizations (Fig. 9). This confidence allows us to focus on a particular level of discretization-related error, indicated by the red band in Fig. 9a. By fixing the number  $N_{\mathcal{W}}$  of sites in each reservoir to a value within this band, we can determine how the singular value threshold  $\epsilon_{\text{min}}$  controls convergence of the current and the system state at a given accuracy. This accommodation also fixes the number of bias window sites  $N_{\mathcal{B}}$  to

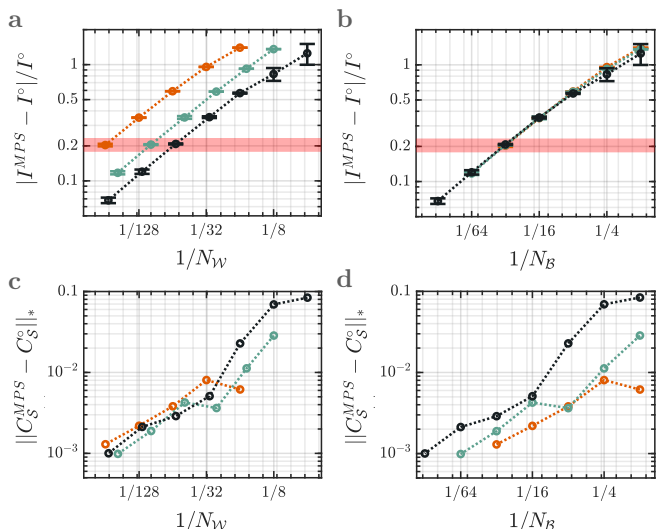


FIG. 9. **Error and discretization for non-interacting MPS.** Convergence of reservoir discretizations for the non-interacting two-site system  $\mathcal{S}$  of Fig. 6, obtained using MPS with a fixed Schmidt cutoff  $\epsilon_{\min} = 10^{-6}$ . Scaling is quantified with respect to the number of modes in each reservoir  $N_W$  and the number of modes within the bias window  $N_B$ . Data correspond to (a, b) relative error in the steady-state current  $I^{MPS} = I[\gamma^*]$  versus the Landauer limit  $I^\circ$  and (c, d) the normalized trace distance between correlation matrix  $C_S^{MPS}$  for  $\mathcal{S}$  and its infinite reservoir counterpart  $C_S^\circ$ . Discretizations follow linear (orange), the linear-logarithmic (green), and the linear-inverse (black) arrangements. The red band in (a, b) is at relative error scale (0.20), for which  $N_W$  is 256, 100, and 60, respectively and  $N_B$  is 32. The current  $I^{MPS}$  is an average from  $\mathcal{L}\mathcal{S}$ ,  $\mathcal{S}_1\mathcal{S}_2$ , and  $\mathcal{S}\mathcal{R}$  interfaces. Uncertainties  $\sigma = \pm\sqrt{\sigma_1^2 + \sigma_2^2}$  reflect fluctuations  $\sigma_1$  of the current over a temporal window  $\Delta t = 50\omega_0^{-1}$ , as well as the mismatch  $\sigma_2^2 = \sum_j |I_j - I^{MPS}|^2/3$  of currents at the interfaces  $j \in \{\mathcal{L}\mathcal{S}_1, \mathcal{S}_1\mathcal{S}_2, \mathcal{S}_2\mathcal{R}\}$ . The designated  $C_S^{MPS}$  is representative of the final simulation time step. Parameters are identical to Fig. 6, but with a system-reservoir coupling  $v_0 = \omega_0/8$ .

be the same for each discretization—an important point that we will address later. To proceed, we measure error with respect to the exact (i.e., with no truncation), finite-size current  $I^R$  associated with a given  $N_W$  and discretization of a non-interacting system. We find a numerical solution that slowly approaches the exact current as  $\epsilon_{\min}$  is decreased, however, this convergence is not uniform (Fig. 10a). The choice of discretization has little impact on convergence (and its numerical cost) even though the number of MPS sites is quite different.

This behavior can be understood by using the quantity  $F = \sum_j D_j^3$  to estimate relative cost of MPS simulations for a given  $\epsilon_{\min}$ . This metric encapsulates the scaling of computational time with bond dimension, as other parameters contributing to the cost (e.g., bond dimensions for the Lindbladian MPO, local Hilbert space dimensions) are the same for all discretizations. Our discretizations differ in the total number of reservoir sites

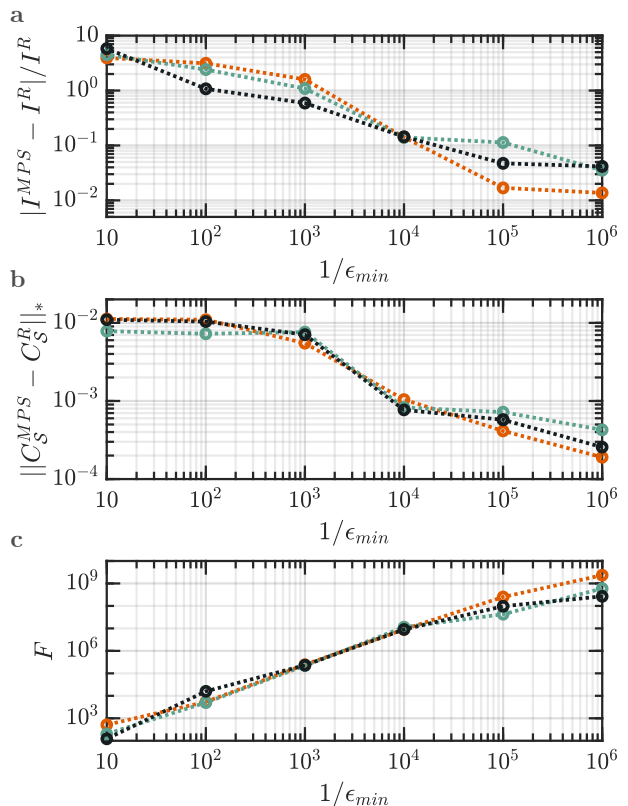


FIG. 10. **Error and Schmidt cutoff for non-interacting MPS.** (a) The relative error in the steady-state current  $I^{MPS}$  compared to reference values  $I^R$  (these reference currents correspond to exact, finite  $N_W$  simulations performed using values of  $N_W$  that give data points demarcated by the red band in Fig. 9(a,b) thus reflecting the  $\epsilon_{\min} \rightarrow 0$  limit).  $I^R$  is at a fixed error level with respect to the continuum current  $I^\circ$ . The convergence is plotted versus the inverse Schmidt cutoff  $1/\epsilon_{\min}$ . (b) The normalized trace distance between the correlation matrix  $C_S^{MPS}$  for  $\mathcal{S}$  and the reference  $C_S^R$  versus  $1/\epsilon_{\min}$ . (c) The relative, approximate numerical cost, versus  $1/\epsilon_{\min}$ , of a single MPS update  $F = \sum_j D_j^3$ , defined in terms of the MPS bond dimensions  $D_j$  at all bipartitions. Discretizations correspond to linear (orange), the linear-logarithmic (green), and the linear-inverse (black) arrangements.

$N_W$  that are needed to reproduce a given level of accuracy. However, an analysis based on  $F$  suggests that the degree of correlation is determined by the number of states within the bias window  $N_B$ , which is the same for each discretization at a given accuracy level (Fig. 10). Thus, we cannot specify a discretization that will yield a clear increase in computational performance for MPS simulations. The only benefit to having a smaller  $N_W$  is having fewer modes outside the bias window. This has little computational impact, as our ordering places these modes near the ends of the MPS, where they require a small  $D_j$  and contribute weakly to  $F$ .

A related analysis can be performed for interacting systems, which we demonstrate by introducing a density-density interaction of strength  $U = -\omega_0/2$  between the

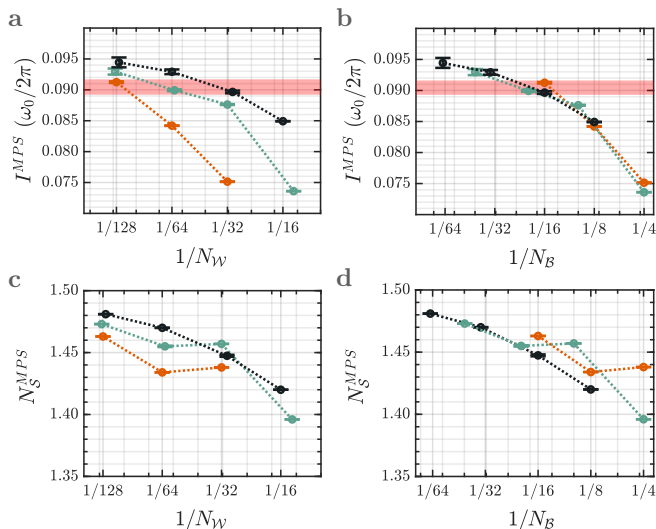


FIG. 11. **Discretization effects for interacting MPS.** Convergence of reservoir discretizations obtained with MPS approach for two-site impurity of Fig. 9 with an additional many-body interaction  $U = -\omega_0/2$ . The behavior is computed versus the number of modes in each reservoir  $N_W$  and the number of modes within each bias window  $N_B$ . Data correspond to (a, b) the steady-state current  $I^{MPS} = I[\gamma_s]$  and (c, d) the total particle number in  $\mathcal{S}$ ,  $N_S^{MPS} = N_S[\gamma_s]$ , where  $\gamma_s$  estimates the best relaxation as described in the text. Discretizations follow linear (orange), the linear-logarithmic (green), and the linear-inverse (black) arrangements. The red band in (a, b) gives the reference current,  $I^R$ , which, by virtue of being approximately the same value of the current, is at the same relative error scale. The number of modes,  $N_W$ , is 128, 62, and 30, and  $N_B$  is 16, 20, and 16 for the three discretizations, respectively. Model parameters and uncertainty calculations in the current are identical to Fig. 9. Uncertainties for  $N_S^{MPS}$  are given by  $\sigma = \pm\sigma_1$ , reflecting fluctuations of the measurement over a temporal window  $\Delta t = 50\omega_0^{-1}$ . These density uncertainties are smaller than the data point size in panels (c, d). The simulations have Schmidt cutoff  $\epsilon_{min} = 10^{-6}$ .

impurity sites. Since the exact solution is unknown, we estimate an optimal relaxation  $\gamma_s$  by comparing  $\gamma$ -dependent turnover profiles with on/off-resonant modes (Fig. 4), as validated earlier in the manuscript. This procedure is executed for each discretization and set of reservoir modes, yielding the scaling behavior presented in Fig. 11a. We again find a current that converges monotonically with increasing  $N_W$  for all discretization schemes, though the convergence of occupations is more variable.

We can also assess how simulation performance scales with  $\epsilon_{min}$  when interactions are present. To avoid finite size effects, we limit this and subsequent analysis to points with  $N_B > 4$ . Following our analysis for the non-interacting MPS, we define a fixed level of discretization-related error. We do so by choosing discretizations which give approximately the same current  $I^R$  (the red band in Fig. 11a) and thus have a similar error with respect to the

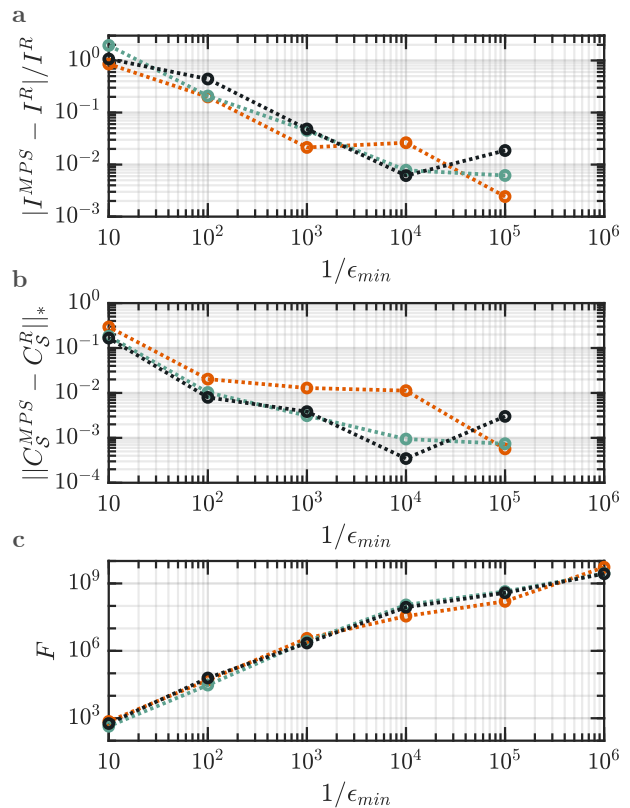


FIG. 12. **Error and Schmidt cutoff for interacting MPS.** (a) The relative error in the steady-state current  $I^{MPS}$  compared to the reference value  $I^R$  (demarcated by the red band in Fig. 11(a,b), which is at a approximately the same value). The convergence is plotted versus the inverse Schmidt cutoff  $1/\epsilon_{min}$ . The reference current  $I^R$  is at the tightest cutoff of  $\epsilon_{min} = 10^{-6}$ . (b) The normalized trace distance between correlation matrix  $C_S^{MPS}$  for  $\mathcal{S}$  and the reference  $C_S^R$  versus  $1/\epsilon_{min}$ . (c) The relative numerical cost, versus  $1/\epsilon_{min}$ , of a single MPS update  $F = \sum_j D_j^3$ , defined in terms of the MPS bond dimensions  $D_j$  at all bipartitions. Discretizations correspond to linear (orange), the linear-logarithmic (green), and the linear-inverse (black) arrangements.

continuum limit. The latter is estimated to be far from distinguished points (as discussed below) but it can't be derived exactly. In addition we quantify truncation-related error measured with respect to the finite-size currents  $I^R$  obtained for  $\epsilon_{min} = 10^{-6}$  at given discretization. We find that convergence of the current and correlation matrix  $C_S$  is comparable across discretizations, as is the numerical cost quantified through  $F$  (Fig. 12c). Once again, performance is dictated by how accurately we represent the bias window (and thus by  $N_B$ ), emulating the non-interacting MPS. The particular reservoir discretization, at comparable  $N_B$ , still has little impact when converging the current in tensor network simulations at practical reservoir sizes. In fact, the Schmidt cutoff  $\epsilon_{min}$  and underlying system Hamiltonian are the primary determinants of convergence and its numerical cost.

The exact, continuum–limit current is unknown for many interesting systems. Nonetheless, our extended reservoir simulations should approach this regime as the number of explicit reservoir modes is increased. This is particularly true for the current, where we have observed monotonic convergence with  $N_W$  in both non–interacting and interacting MPS simulations. Below we propose a fitting procedure to estimate the continuum limit current using a simple scaling law. We test our procedure with non–interacting calculations and apply it to the interacting model.

The importance of bias window modes is captured by parameterizing the scaling law in terms of  $N_B$ ,  $I = I^\infty + A/N_B^p$ , where  $I^\infty$ ,  $A$ , and  $p$  are fit parameters.  $I^\infty$  provides an estimate for the continuum limit current  $I^\circ$ . We test the fitting procedure by applying it to MPS data for non–interacting model in Fig. 9b. The fit for each discretization separately gives scaling exponents of  $p = [0.48 \pm 0.05, 0.54 \pm 0.04, 0.67 \pm 0.02]$  and estimates for the continuum limit current  $2\pi I^\infty/\omega_0 = [0.0023 \pm 0.0003, 0.0026 \pm 0.0002, 0.0030 \pm 0.0001]$  for the linear, linear–logarithmic, and linear–inverse discretizations, respectively. These exhibit reasonable agreement with their exact counterpart  $2\pi I^\circ/\omega_0 = 0.0031$ , albeit with some discrepancies. The high performance of the linear–inverse arrangement is expected since bias window modes predominate for this discretization.

Given that the currents from different discretizations overlap when plotted versus  $1/N_B$ , we can aggregate the data sets to increase the total number of data points and also change the fit range to be  $N_B > 4$ . A collective fit to this aggregated data gives us a scaling exponent  $p = 0.72 \pm 0.02$  and an estimate for the continuum current of  $2\pi I^\infty/\omega_0 = 0.0030 \pm 0.0001$ . This is in good agreement with  $I^\circ$ . The MPS scaling exponents  $p$  can be compared to the exact finite  $N_W$  profiles in Fig. 6, which includes many more points than accessible with MPS. We assume that they give an exact estimate  $I^\infty = I^\circ$ . The fit for each discretization separately gives scaling exponents of  $p = [0.77 \pm 0.01, 0.77 \pm 0.01, 0.74 \pm 0.01]$  for the linear, linear–logarithmic and linear–inverse discretizations, respectively and  $p = 0.76 \pm 0.01$  for collective fit. This suggests that the collective fit for the aggregated MPS data is yielding better results.

The same strategy can be applied to the interacting system of Fig. 11. Since we have a very limited data set, we aggregate the data from different discretizations. The collective fit gives  $p = 1.50 \pm 0.63$  and  $2\pi I^\infty/\omega_0 = 0.093 \pm 0.002$ . The large standard error in the exponent may be due to a few factors: non–scaling finite–size effects, other contributions to numerical uncertainty, or that modes outside the bias window have a greater influence when interactions are present. The outer modes influence densities and in turn affect the current, which may be increasing their importance.

## VI. CONCLUSIONS

Our observations suggest a general approach when using discrete reservoirs in quantum transport simulations. In a technical sense, we find that the linear–inverse discretization is the most efficient arrangement for non–interacting cases, particularly when combined with a relaxation method based on the level spacing in the bias window. Nonetheless, the performance between discretizations is not dramatic, and is effectively negligible for the  $N_W$  used in practical simulations. This is especially true for interacting MPS–based simulations, where correlations ultimately regulate the computational cost. Despite this behavior, one should remain mindful of cases where the choice of discretization can become more important—notably for small  $N_W$  or at a small bias where a large portion of the bandwidth becomes less relevant (at least for the current). The importance of this limit has been recognized by other authors, particularly in the context of numerical renormalization group calculations [66–70]. Furthermore, there may remain some interplay between the performance of a given discretization toward a particular observable and the distribution of states within  $\mathcal{S}$ . This consideration could be relevant in computationally taxing cases, including certain many–body limits, where  $N_W$  is strongly limited by practical constraints.

In addition, we developed a method for estimating the optimal relaxation  $\gamma^*$  that approximates the continuum result  $I(\gamma^*) \approx I^\circ$ . This is valuable when the continuum limit  $I^\circ$  is unknown. While the turnover region will vary between model Hamiltonians and coupling regimes, we need only “switch on” a level shift between reservoirs and use the intersection  $\gamma_s$  between shifted and unshifted turnover profiles (or  $\gamma_\ell$  from linear extrapolation) to estimate the best relaxation. This provides a practical tool for performing extended reservoir simulations with matrix product states and tensor networks.

## VII. SUPPLEMENTARY MATERIAL

The supplementary material contains turnover and scaling analyses for additional multi–site systems.

## VIII. ACKNOWLEDGEMENTS

J. E. E. acknowledges support under the Cooperative Research Agreement between the University of Maryland and the National Institute for Standards and Technology Physical Measurement Laboratory, Award 70NANB14H209, through the University of Maryland. We acknowledge support by the National Science Center (NCN), Poland under Projects No. 2016/23/B/ST3/00839 (G. W.) and No. 2020/38/E/ST3/00150 (M. M. R.).

## IX. DATA AVAILABILITY

The data that supports the findings of this study are available within the article and its supplementary material.

- 
- [1] J. Maassen, M. Harb, V. Michaud-Rioux, Y. Zhu, and H. Guo, *Proc. IEEE* **101**, 518 (2013).
- [2] S. Kurth and G. Stefanucci, *J. Phys.: Condens. Matter* **29**, 413002 (2017).
- [3] M. Thoss and F. Evers, *J. Chem. Phys.* **148**, 030901 (2018).
- [4] R. Härtle, G. Cohen, D. R. Reichman, and A. J. Millis, *Phys. Rev. B* **92**, 085430 (2015).
- [5] I. Krivenko, J. Kleinhenz, G. Cohen, and E. Gull, *Phys. Rev. B* **100**, 201104 (2019).
- [6] M. Ridley, M. Galperin, E. Gull, and G. Cohen, *Phys. Rev. B* **100**, 165127 (2019).
- [7] M. M. Rams and M. Zwolak, *Phys. Rev. Lett.* **124**, 137701 (2020).
- [8] G. Wójtowicz, J. E. Elenewski, M. M. Rams, and M. Zwolak, *Phys. Rev. A* **101**, 050301 (2020).
- [9] M. Brenes, J. J. Mendoza-Arenas, A. Purkayastha, M. T. Mitchison, S. R. Clark, and J. Goold, *Phys. Rev. X* **10**, 031040 (2020).
- [10] M. Lotem, A. Weichselbaum, J. von Delft, and M. Goldstein, *Phys. Rev. Research* **2**, 043052 (2020).
- [11] D. M. Fugger, D. Bauernfeind, M. E. Sorantin, and E. Arrigoni, *Phys. Rev. B* **101**, 165132 (2020).
- [12] A. Dorda, M. Nuss, W. von der Linden, and E. Arrigoni, *Phys. Rev. B* **89**, 165105 (2014).
- [13] A. Dorda, M. Ganahl, H. G. Evertz, W. von der Linden, and E. Arrigoni, *Phys. Rev. B* **92**, 125145 (2015).
- [14] F. Schwarz, M. Goldstein, A. Dorda, E. Arrigoni, A. Weichselbaum, and J. von Delft, *Phys. Rev. B* **94**, 155142 (2016).
- [15] D. M. Fugger, A. Dorda, F. Schwarz, J. v. Delft, and E. Arrigoni, *New J. Phys.* **20**, 013030 (2018).
- [16] D. Gruss, K. A. Velizhanin, and M. Zwolak, *Sci. Rep.* **6**, 24514 (2016).
- [17] J. E. Elenewski, D. Gruss, and M. Zwolak, *J. Chem. Phys.* **147**, 151101 (2017).
- [18] D. Gruss, A. Smolyanitsky, and M. Zwolak, *J. Chem. Phys.* **147**, 141102 (2017).
- [19] D. Gruss, A. Smolyanitsky, and M. Zwolak, *arXiv:1804.02701* (2018).
- [20] M. Zwolak, *J. Chem. Phys.* **153**, 224107 (2020).
- [21] M. Zwolak, *arXiv:2009.04466* (2020).
- [22] G. Wójtowicz, J. E. Elenewski, M. M. Rams, and M. Zwolak, *Phys. Rev. B* **104**, 165131 (2021).
- [23] W. Kohn and J. M. Luttinger, *Phys. Rev.* **108**, 590 (1957).
- [24] W. R. Frensley, *J. Vac. Sci. Technol. B* **3**, 1261 (1985).
- [25] W. R. Frensley, *Rev. Mod. Phys.* **62**, 745 (1990).
- [26] H. Mizuta and C. J. Goodings, *J. Phys.: Condens. Matter* **3**, 3739 (1991).
- [27] M. V. Fischetti, *J. Appl. Phys.* **83**, 270 (1998).
- [28] M. V. Fischetti, *Phys. Rev. B* **59**, 4901 (1999).
- [29] I. Knezevic and B. Novakovic, *J. Comput. Electron.* **12**, 363 (2013).
- [30] A. A. Dzhioev and D. S. Kosov, *J. Chem. Phys.* **134**, 044121 (2011).
- [31] O. Hod, C. A. Rodríguez-Rosario, T. Zelovich, and T. Frauenheim, *J. Phys. Chem. A* **120**, 3278 (2016).
- [32] T. Zelovich, L. Kronik, and O. Hod, *J. Chem. Theory Comput.* **10**, 2927 (2014).
- [33] T. Zelovich, L. Kronik, and O. Hod, *J. Chem. Theory Comput.* **11**, 4861 (2015).
- [34] T. Zelovich, L. Kronik, and O. Hod, *J. Phys. Chem. C* **120**, 15052 (2016).
- [35] T. Zelovich, T. Hansen, Z.-F. Liu, J. B. Neaton, L. Kronik, and O. Hod, *J. Chem. Phys.* **146**, 092331 (2017).
- [36] U. N. Morzan, F. F. Ramírez, M. C. González Lebrero, and D. A. Scherlis, *J. Chem. Phys.* **146**, 044110 (2017).
- [37] F. Ramírez, D. Dundas, C. G. Sánchez, D. A. Scherlis, and T. N. Todorov, *J. Phys. Chem. C* **123**, 12542 (2019).
- [38] T.-M. Chiang and L.-Y. Hsu, *J. Chem. Phys.* **153**, 044103 (2020).
- [39] A. Oz, O. Hod, and A. Nitzan, *J. Chem. Theory Comput.* **16**, 1232 (2020).
- [40] A. Jovchev and F. B. Anders, *Phys. Rev. B* **87**, 195112 (2013).
- [41] F. Schwarz, I. Weymann, J. von Delft, and A. Weichselbaum, *Phys. Rev. Lett.* **121**, 137702 (2018).
- [42] M. Zwolak, *J. Chem. Phys.* **129**, 101101 (2008).
- [43] F. Chen, G. Cohen, and M. Galperin, *Phys. Rev. Lett.* **122**, 186803 (2019).
- [44] F. Chen, M. I. Katsnelson, and M. Galperin, *Phys. Rev. B* **101**, 235439 (2020).
- [45] E. Arrigoni, M. Knap, and W. von der Linden, *Phys. Rev. Lett.* **110**, 086403 (2013).
- [46] Y. Meir and N. S. Wingreen, *Phys. Rev. Lett.* **68**, 2512 (1992).
- [47] A.-P. Jauho, N. S. Wingreen, and Y. Meir, *Phys. Rev. B* **50**, 5528 (1994).
- [48] J. Zhou, K. Wang, B. Xu, and Y. Dubi, *J. Am. Chem. Soc.* **140**, 70 (2018).
- [49] In the continuum limit, the current through the system,  $I = (2\pi)^{-1} \int d\omega [f_{\mathcal{L}}(\omega) - f_{\mathcal{R}}(\omega)] \text{tr} [\mathbf{\Gamma}^{\mathcal{L}} \mathbf{G}^r \mathbf{\Gamma}^{\mathcal{R}} \mathbf{G}^a]$ , is defined by the retarded (advanced) Green's functions for the system  $\mathbf{G}^{r(a)} = [\omega - \bar{\mathbf{H}} - \mathbf{\Sigma}_{S\mathcal{L}}^{r(a)} - \mathbf{\Sigma}_{S\mathcal{R}}^{r(a)}]^{-1}$ , the spectral densities  $\mathbf{\Gamma}^{\mathcal{L}(\mathcal{R})} = -2\text{Im} \mathbf{\Sigma}_{S\mathcal{L}(\mathcal{SR})}^r$ , and the biased Fermi-Dirac distributions  $f_{\mathcal{L}(\mathcal{R})}$  in each reservoir. Here the self-energy  $(\mathbf{\Sigma}_{S\mathcal{L}}^{r(a)})_{ij}(\omega) = v_i v_j G_{\mathcal{L}}^{r(a)}(\omega)$  of the system due to  $\mathcal{L}$  is related to the reservoir Green's functions  $G_{\mathcal{L}}^{r(a)}(\omega) = [\omega - \Sigma_{\mathcal{L}}^{r(a)}(\omega)]^{-1}$  through the coupling  $v_i$  between the  $i$ -th system site and the reservoir's terminal site. In this context,  $\Sigma_{\mathcal{L}}^{r(a)}(\omega) = [\omega \mp i\sqrt{\mathcal{W}^2/4 - \omega^2}]/2$  is the self-energy of a semi-infinite, one-dimensional reservoir. An identical set of expressions holds for  $\mathbf{\Sigma}_{S\mathcal{R}}^{r(a)}$ .
- [50] R. Bulla, T. A. Costi, and T. Pruschke, *Rev. Mod. Phys.* **80**, 395 (2008).

- [51] Explicitly, the midpoint coupling for the reservoir mode at  $\omega_k$  is derived to match the spectral density in the thermodynamic limit (i.e., reservoirs which are a continuum of states) at the midpoint of an interval  $\omega_k \pm \Delta_k/2$ , yielding  $v_k = [4v_0^2\Delta_k\sqrt{1-(2\omega_k/\mathcal{W})^2}/\mathcal{W}\pi]^{1/2}$ . Conversely, the integrated coupling maintains the total spectral weight from the continuum reservoirs within the interval  $\omega_k \pm \Delta_k/2$ , which gives  $v_k = v_0\pi^{1/2}[K(\omega_k + \Delta_k/2) - K(\omega_k - \Delta_k/2)]^{1/2}$ , as defined in terms of the quantity  $K(\omega) = 2\omega(1-4\omega^2/\mathcal{W}^2)^{1/2}/\mathcal{W} + \csc^{-1}(\mathcal{W}/2\omega)$ . Here,  $v_0$  is the system-reservoir coupling in the thermodynamic limit.
- [52] H. Kramers, *Physica* **7**, 284 (1940).
- [53] K. A. Velizhanin, C.-C. Chien, Y. Dubi, and M. Zwolak, *Phys. Rev. E* **83**, 050906 (2011).
- [54] C.-C. Chien, K. A. Velizhanin, Y. Dubi, and M. Zwolak, *Nanotechnology* **24**, 095704 (2013).
- [55] K. A. Velizhanin, S. Sahu, C.-C. Chien, Y. Dubi, and M. Zwolak, *Sci. Rep.* **5**, 17506 (2015).
- [56] C.-C. Chien, S. Kouachi, K. A. Velizhanin, Y. Dubi, and M. Zwolak, *Phys. Rev. E* **95**, 012137 (2017).
- [57] C.-C. Chien, K. A. Velizhanin, Y. Dubi, B. R. Ilic, and M. Zwolak, *Phys. Rev. B* **97**, 125425 (2018).
- [58] M. A. Nielsen and I. L. Chuang, *Quantum Computation and Quantum Information* (Cambridge University Press, Cambridge, 2010).
- [59] The current is often only a small contribution to the trace distance. For the cases we examined, the relaxation that optimizes the trace distance comes at a smaller relaxation strength than that which optimizes the current.
- [60] We can uniquely define  $\gamma_s$  only when the two curves intersect. This is the case in all the models that we study here. They do not, however, always share a common large- $\gamma$  regime. It is unknown whether the intersection always happens.
- [61] There is a clear tension between the optimum for a particular observable (current in this case) and for the whole system state. Current is only a small component of the whole system state here, making this tension readily apparent.
- [62] F. A. Wolf, I. P. McCulloch, and U. Schollwöck, *Phys. Rev. B* **90**, 235131 (2014).
- [63] M. Zwolak and G. Vidal, *Phys. Rev. Lett.* **93**, 207205 (2004).
- [64] F. Verstraete, J. J. García-Ripoll, and J. I. Cirac, *Phys. Rev. Lett.* **93**, 207204 (2004).
- [65] J. Haegeman, C. Lubich, I. Oseledets, B. Vandereycken, and F. Verstraete, *Phys. Rev. B* **94**, 165116 (2016).
- [66] V. L. Campo, Jr. and L. N. Oliveira, *Phys. Rev. B* **72**, 104432 (2005).
- [67] R. Žitko and T. Pruschke, *Phys. Rev. B* **79**, 085106 (2009).
- [68] M. Ganahl, P. Thunström, F. Verstraete, K. Held, and H. G. Evertz, *Phys. Rev. B* **90**, 045144 (2014).
- [69] Y. L. Abd M. Höppner, O. Gunnarsson, and M. W. Haverkort, *Phys. Rev. B* **90**, 085102 (2014).
- [70] A. Braun and P. Schmitteckert, *Phys. Rev. B* **90**, 165112 (2014).

**Supplementary Information for “Performance of Reservoir Discretizations in  
Quantum Transport Simulations”**

Justin E. Elenewski

*Biophysical and Biomedical Measurement Group,  
Microsystems and Nanotechnology Division, Physical Measurement Laboratory,  
National Institute of Standards and Technology, Gaithersburg, MD, USA and  
Institute for Research in Electronics and Applied Physics,  
University of Maryland, College Park, MD, USA*

Gabriela Wójtowicz and Marek M. Rams\*

*Jagiellonian University, Institute of Theoretical Physics, Lojasiewicza 11, 30-348 Kraków, Poland*

Michael Zwolak<sup>†</sup>

*Biophysical and Biomedical Measurement Group,  
Microsystems and Nanotechnology Division, Physical Measurement Laboratory,  
National Institute of Standards and Technology, Gaithersburg, MD, USA*

**CONTENTS**

Convergence of the Linear Extrapolation Estimator	3
Current Estimators in Diverse Coupling and Relaxation Regimes	4
Non-Interacting Single-Site Impurity at Weak System-Reservoir Coupling	4
Estimators for the Non-interacting Two-Site Impurity at Weak System-Reservoir Coupling	7
Non-interacting two-site impurity at Strong System-Reservoir Coupling	8
Three-Site Model	13
Alternative Linear-Logarithmic Discretizations	16
Method I	16
Method II	18
References	21

CONVERGENCE OF THE LINEAR EXTRAPOLATION ESTIMATOR

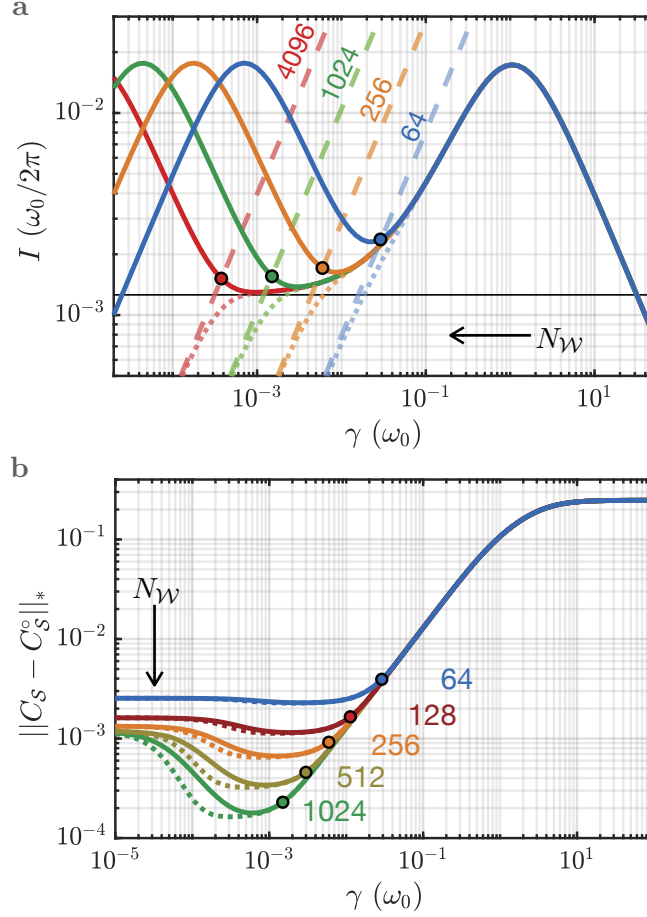


FIG. S1. **Turnover and the linear extrapolation estimator.** (a) Turnover in the steady-state current  $I$  for the non-interacting, dual-site model of Fig. 4 in the primary manuscript. The on-resonant (solid) and off-resonant (dotted) profiles are shown, along with a linear extrapolation of the off-resonant turnover  $\gamma$  (dashed) into the on-resonant turnover. These profiles intersect at the linear extrapolation estimator  $\gamma_\ell$ . The relaxation  $\gamma_\ell$  settles into the low-to-moderate  $\gamma$  shoulder of the virtual anomaly at large  $N_W$ , leading to the saturation seen in Fig. 4. (b) Turnover of the normalized trace distance between the system correlation matrix  $C_S$  and its continuum reservoir counterpart  $C_S^c$ . The estimator  $\gamma_\ell$  is again shown as a circle, which rides a growing minimum in trace distance as  $N_W$  is increased. This implies a scaling profile that does not saturate, as captured by Fig. 4c. The dotted line depicts this trace distance for the real part of  $C_S$ , indicating that current-carrying correlations contribute weakly to the error near  $\gamma_\ell$  or  $\gamma^*$ . Parameters in (a) and (b) are identical to Fig. 4 in the primary manuscript.

## CURRENT ESTIMATORS IN DIVERSE COUPLING AND RELAXATION REGIMES

In this extended discussion, we consider several multi-site models for the system  $\mathcal{S}$  and quantify their transport characteristics in an extended reservoir framework. In particular, we demonstrate that our intersection ( $\gamma_s$ ) and linear extrapolation ( $\gamma_\ell$ ) estimators for the optimal transport regime  $\gamma^*$  remain applicable under a broad range of parameters. This underscores their general utility for locating the physical transport regime, particularly when the turnover profiles have an ambiguous plateau architecture.

### Non-Interacting Single-Site Impurity at Weak System-Reservoir Coupling

The single-site impurity corresponds to a canonical quantum impurity problem (Fig. 1b). Here, a single mode in  $\mathcal{S}$  is proportionally coupled to left ( $\mathcal{L}$ ) and right ( $\mathcal{R}$ ) extended reservoirs with strength  $v$ . The system Hamiltonian takes a simple form in terms of  $\omega_1$ , the on-site system frequency:

$$H_{\mathcal{S}} = \hbar\omega_1 c_1^\dagger c_1. \quad (\text{S1})$$

In this case, the  $\gamma$ -dependent turnover mimics the dual-site model from the primary manuscript (Fig. S2). Using the linear discretization as a reference, we find an increasingly wide physical ‘domain of confidence’ between virtual and Markovian anomalies as the number  $N_{\mathcal{W}}$  of explicit reservoir modes is increased. The virtual anomaly also vanishes when modes in  $\mathcal{L}$  and  $\mathcal{R}$  are taken out of resonance, making our  $\gamma_\ell$  and  $\gamma_s$  estimators applicable. Taking advantage of this, we find that the intersection estimator  $\gamma_s$  is a good predictor for the optimal transport regime  $\gamma^*$  (Fig. S3). We can also quantify convergence of the current at  $\gamma^*$  using other discretizations. In doing so, we find that the discretizations perform similarly for the one-site (Fig. S4) and two-site impurities (Fig. S5) in the weak-coupling limit. This agreement does not extend to on-site densities, where there are discrepancies at small  $N_{\mathcal{W}}$  (the linear-logarithmic discretization performs poorly in this regime). Nonetheless, the discretizations remain comparable when  $N_{\mathcal{W}}$  is large (greater than  $N_{\mathcal{W}} \approx 128$  sites).

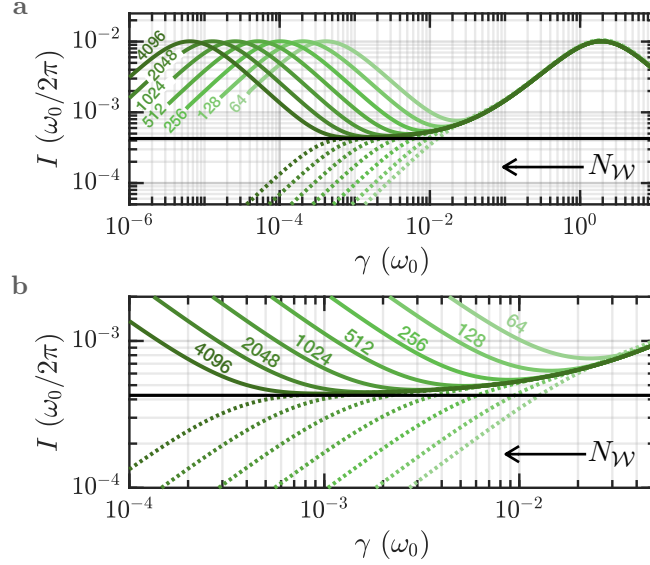


FIG. S2. **Kramers' turnover for the single-site impurity.** (a) Turnover in the steady-state current  $I$  of the non-interacting single-site impurity model from Eq. (S1). The extended reservoirs have a linear discretization and the relaxation  $\gamma_k = \gamma$  is mode independent. Scaling is assessed with respect to the number  $N_{\mathcal{W}}$  of explicit modes in each reservoir for both on-resonant (solid) and off-resonant (dashed; with a level shift) configurations. (b) Inset of the data from (a) near the physical regime. The Landauer limit  $I^\circ$  for continuum reservoirs is shown by the solid, black horizontal line. Calculations are presented with an on-site frequency  $\omega_1 = \omega_0$  and weak system-reservoir coupling  $v = \omega_0/10$ , with a bias of  $\mu = \omega_0/2$  between  $\mathcal{L}$  and  $\mathcal{R}$  and a temperature  $k_B T = \omega_0/40$  for reservoir Fermi distributions. The coupling between system and reservoir sites is provided by the integrated approach (as described in the primary text).

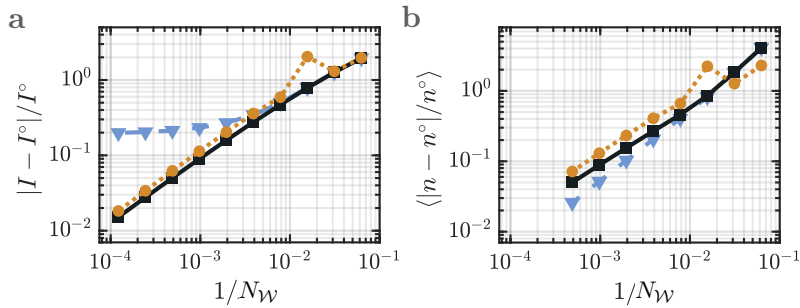
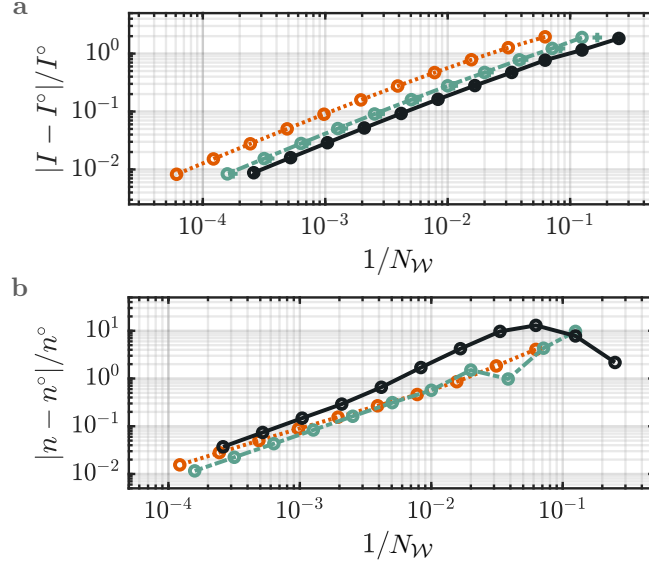


FIG. S3. **Relaxation estimators for the single-site impurity.** Convergence of (a) the current error  $|I - I^\circ|/I^\circ$  and (b) error in the on-site density  $|n - n^\circ|/n^\circ$  with respect to  $N_{\mathcal{W}}$  for our single-site impurity. Scaling profiles correspond to  $\gamma_k = \gamma^*$  (black square), the linear extrapolation estimator  $\gamma_\ell$  (blue triangle), and the intersection of shifted/unshifted turnover profiles  $\gamma_s$  (tan circle). Model parameters are identical to Fig. S2, with a linear discretization and integrated system-reservoir couplings. Error is measured with respect to currents  $I^\circ$  and on-site densities  $n_i^\circ$  in the continuum reservoir limit.



**FIG. S4. Error and discretization for the single-site impurity.** Convergence of reservoir discretizations for our single-site impurity (Fig. S2) when increasing the number  $N_W$  of explicit reservoir sites. This behavior is quantified through (a) relative error in the steady-state current  $I$  and (b) relative error in the on-site density  $n_i$  within  $\mathcal{S}$ . These observables are evaluated at  $\gamma^*$ , as defined in the primary manuscript, and the reference current  $I^\circ$  is the Landauer limit for continuum reservoirs. Discretizations correspond to the standard linear (orange dotted line), the linear-logarithmic (green dashed line), and the linear-inverse (black solid line) arrangements. Results are also provided for additional linear-logarithmic and linear-inverse discretizations which are the transform of a 1D spatial lattice to the energy basis (green and black crosses). Model parameters are identical to those of Fig. S2.

## Estimators for the Non-interacting Two-Site Impurity at Weak System-Reservoir Coupling

We previously quantified the convergence of reservoir discretizations for a non-interacting two-site impurity at weak-coupling (Fig. 6 of the primary manuscript). This analysis may be repeated by using  $\gamma_s$  to estimate the optimal relaxation regime  $\gamma^*$ . In doing so, we find that the distinction between discretizations becomes even less apparent. Nonetheless,  $\gamma_s$  gives a robust estimate irrespective of context (Fig. S5), supporting its use with many-body impurities.

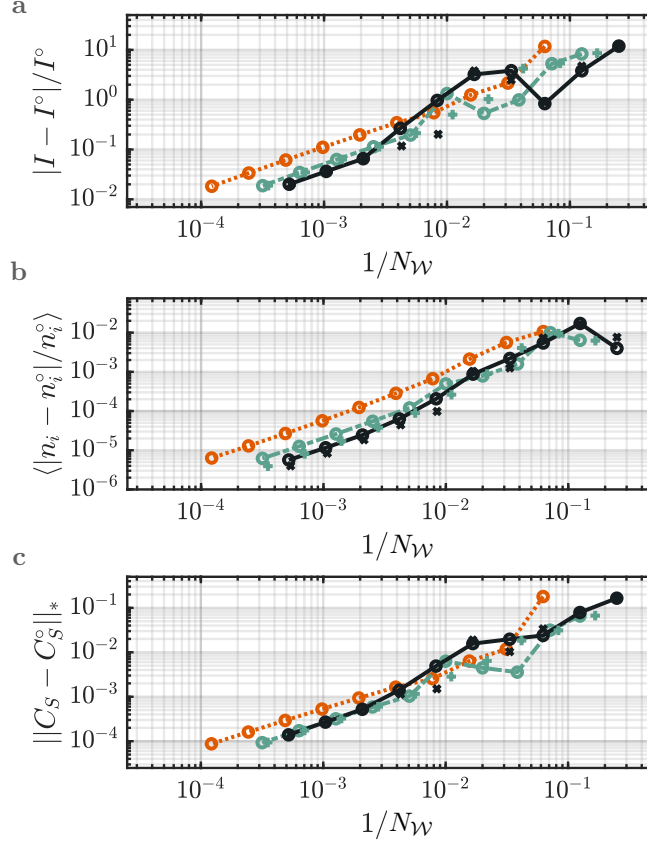


**FIG. S5. Validation of the intersection estimator across discretizations.** The intersection estimator  $\gamma_s$  is used to approximate the optimal relaxation regime  $\gamma^*$  in an analysis parallel to Fig. 6 of the primary manuscript. Convergence is shown for our weakly-coupled ( $v = \omega_0/10$ ) two-site impurity (Fig. S2) when increasing the number  $N_W$  of explicit reservoir sites. This behavior is quantified through (a) relative error in the steady-state current  $I$ ; (b) relative error in the on-site density  $n_i$  within  $\mathcal{S}$ ; and (c) trace distance of the system correlation matrix  $C_S$  and its continuum reservoir counterpart  $C_S^\circ$ . Discretizations correspond to the standard linear (orange dotted line), the linear-logarithmic (green dashed line), and the linear-inverse (black solid line) arrangements. Results are also provided for additional linear-logarithmic and linear-inverse discretizations which are the transform of a 1D spatial lattice to the energy basis (green and black crosses). Parameters, methodology, and labels are otherwise identical to those of Fig. 6.

### Non-interacting two-site impurity at Strong System-Reservoir Coupling

Our primary analysis was performed for a non-interacting, two-site impurity at weak system-reservoir coupling ( $v = \omega_0/10$ ). It is instructive to analyze the same system when the coupling is strong ( $v = \omega_0/2$ ) and the turnover becomes markedly different (Fig. S6). At weak coupling, our single- and double-site systems have a well-defined valley between current turnover anomalies. The bottom of this feature approaches the continuum-limit  $I^\circ$  at the optimal relaxation  $\gamma^*$  and broadens as  $N_{\mathcal{W}}$  is increased. The behavior changes at strong coupling, where there is now a flat turnover plateau that intersects  $I^\circ$  so that  $I(\gamma^*) = I^\circ$  exactly. This regime is difficult to identify by visual inspection due to a lack of prominent plateau features (Fig. S6b), though it does lie at the small- $\gamma$  side due to a weak virtual anomaly.

Despite the change in plateau architecture, the intersection estimator  $\gamma_s$  remains robust and applicable (Fig. S7). In fact, this estimator affords currents  $I(\gamma_s)$  that steadily approach the continuum reservoir limit  $I^\circ$  as  $N_{\mathcal{W}}$  is increased. The linear extrapolation estimator  $\gamma_\ell$  consistently underestimates the current, intersecting the turnover near the mid-plateau upturn (as we move toward smaller  $\gamma$ ) that is associated with the virtual anomaly. Interestingly, this estimator performs poorly for the on-site densities  $n_i$ , with an error that has already saturated at small  $N_{\mathcal{W}}$ . Similar behavior is seen when using  $C_S$  as a measure for the full state of the system. Linear extrapolation from the off-resonant profile now intersects the on-resonant plateau at a point away from the strong downturn regime captured in Fig. S1b.

The estimator  $\gamma_s$  also delivers robust performance for different discretizations at strong coupling, as shown in Fig. S8. That is, all mode arrangements accurately assess key physical quantities. Although currents are formally exact for the optimal estimator  $\gamma^*$  in this strongly-coupled limit, we can nonetheless compare to mean errors of the densities and correlation matrices calculated at  $\gamma^*$ . In doing so, we observe favorable performance in  $\gamma_s$  when estimating  $\gamma^*$  in terms of both error magnitude and the suitability of different discretizations (Fig. S9).

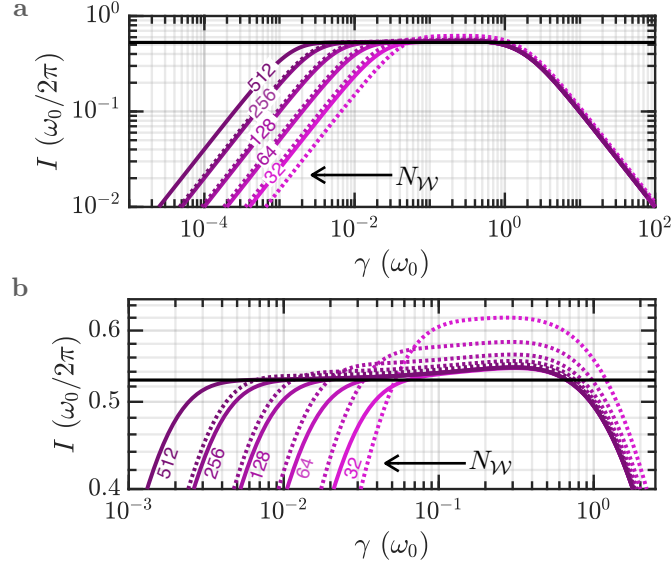
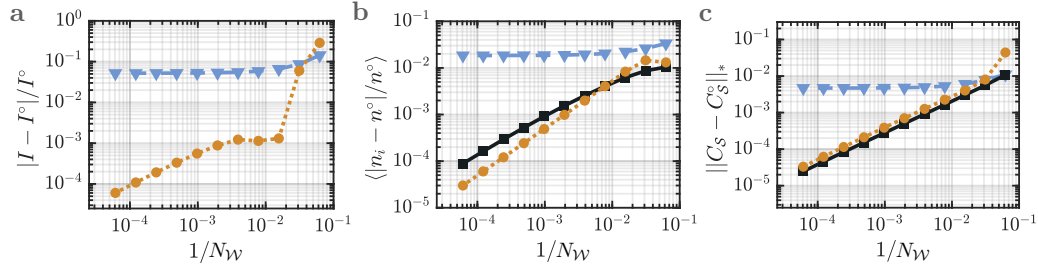


FIG. S6. **Kramers' turnover for the strongly-coupled two-site impurity.** (a) Turnover in the steady-state current  $I$  of the non-interacting two-site impurity model from Fig 3b of the primary manuscript, but now at strong  $\mathcal{S} - \mathcal{LR}$  coupling. The extended reservoirs have a linear discretization and the relaxation  $\gamma_k = \gamma$  is mode independent. Scaling is assessed with respect to the number  $N_W$  of explicit modes in each reservoir for both on-resonant (solid) and off-resonant (dashed; with a level shift) configurations. (b) Inset of the data from (a) near the physical regime. The Landauer limit  $I^\circ$  for continuum reservoirs is shown by the solid, black horizontal line. Calculations are presented with on-site frequencies  $\omega_{\mathcal{S},j} = 0 \cdot \omega_0$ , a coupling of  $v_{12} = (1 + \sqrt{2})\omega_0/4$  between system sites, and strong  $\mathcal{S} - \mathcal{LR}$  coupling  $v = \omega_0/2$ . A bias of  $\mu = \omega_0/2$  is applied between  $\mathcal{L}$  and  $\mathcal{R}$  and a temperature  $k_B T = \omega_0/40$  is used for reservoir Fermi distributions. Couplings are provided by the integrated approach.



**FIG. S7. Relaxation estimators for the strongly coupled two-site impurity.** Convergence of (a) the current error  $|I - I^\circ|/I^\circ$ ; (b) the mean error of the on-site density  $\langle |n_i - n_i^\circ|/n_i^\circ \rangle$ ; and (c) the normalized trace distance between the system correlation matrix  $C_S$  and its continuum reservoir counterpart  $C_S^\circ$ . Scaling is provided with respect to the number of explicit modes in each reservoir  $N_W$  and estimated using  $\gamma_k = \gamma^*$  (black square), the linear extrapolation estimator  $\gamma_\ell$  (blue triangle), and the intersection of shifted/unshifted turnover profiles  $\gamma_s$  (tan circle). Model parameters are identical to Fig. S6, with a linear discretization and integrated system-reservoir couplings. Error is measured with respect to currents  $I^\circ$  and on-site densities  $n_i^\circ$  in the Landauer limit of continuum reservoirs. The  $I(\gamma^*)$  scaling is not provided for (a) since the plateau intersects the Landauer limit and thus the result will be (incidentally) exact.

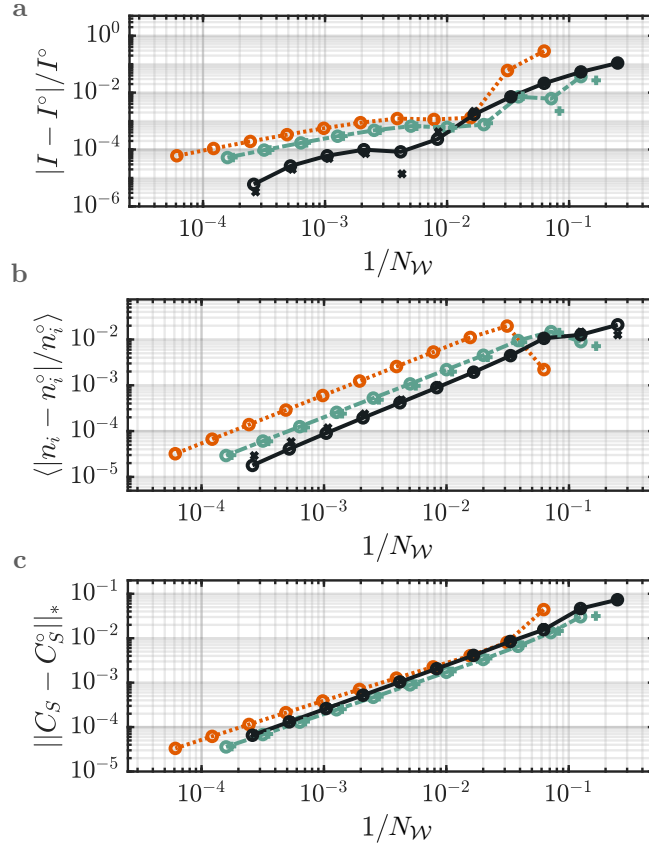


FIG. S8. **Estimator validation across discretizations for the strongly coupled two-site impurity.**

The intersection estimator  $\gamma_s$  is used to approximate the optimal relaxation regime  $\gamma^*$  in an analysis that parallels Fig. 6 of the primary manuscript. Convergence is shown for our strongly-coupled ( $v = \omega_0/2$ ) two-site impurity (Fig. S2) when increasing the number  $N_W$  of explicit reservoir sites. This behavior is quantified through (a) relative error in the steady-state current  $I$ ; (b) relative error in the mean on-site density  $n_i$  within  $\mathcal{S}$ ; and (c) the trace between the system correlation matrix  $C_S$  and its continuum reservoir counterpart  $C_S^o$ . The reference values ( $I^o$ ,  $n_i^o$  and  $C_S^o$ ) are taken in the continuum reservoir limit. Discretizations correspond to the standard linear (orange, dotted line), the linear-logarithmic (green, dashed line), and the linear-inverse (black solid line) arrangements. Results are also provided for additional linear-logarithmic and linear-inverse discretizations which are the transform of a 1D spatial lattice to the energy basis (green and black crosses). Parameters, methodology, and labels are otherwise identical to those of Fig. 6.

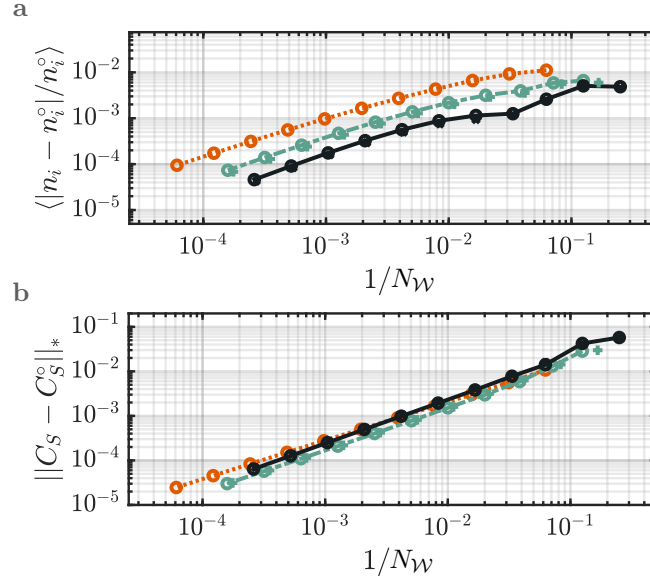


FIG. S9. **Error and discretization for the strongly coupled two-site impurity.** Convergence of reservoir discretizations for our two-site impurity (Fig. S2) when increasing the number  $N_{\mathcal{W}}$  of explicit reservoir sites at strong  $\mathcal{S}$ - $\mathcal{LR}$  coupling ( $v = \omega_0/2$ ). These observables are evaluated at  $\gamma^*$ , as defined in the primary manuscript. This behavior is quantified through (a) relative error in the on-site density  $n_i$  within  $\mathcal{S}$  and (b) the normalized trace distance between the system correlation matrix  $C_{\mathcal{S}}$  and its continuum reservoir counterpart  $C_{\mathcal{S}}^{\circ}$ . The reference values ( $n_i^{\circ}$  and  $C_{\mathcal{S}}^{\circ}$ ) are taken in the continuum reservoir limit. Discretizations correspond to the standard linear (orange, dotted line), the linear-logarithmic (green, dashed line), and the linear-inverse (black solid line) arrangements. Results are also provided for additional linear-logarithmic and linear-inverse discretizations which are the transform of a 1D spatial lattice to the energy basis (green and black crosses). Model parameters are identical to those of Fig. 6.

### Three-Site Model

The three-site impurity is a more complex case, corresponding to a linear chain of sequentially-coupled sites. These connect to the semi-infinite reservoir  $\mathcal{L}$  at the first site of the chain and to the reservoir  $\mathcal{R}$  at the last site. The Hamiltonian for this arrangement reads

$$H_S = \sum_{j=1}^3 \hbar\omega_j c_j^\dagger c_j + \hbar v_{12} (c_1^\dagger c_2 + \text{h.c.}) + \hbar v_{23} (c_2^\dagger c_3 + \text{h.c.}) \quad (\text{S2})$$

which, in essence, is a three-site tight-binding model. For simplicity, we adopt on-site energies of  $\omega_j = 0 \cdot \omega_0$ , system-site couplings  $v_{12} = v_{23} = (1 + \sqrt{2})\omega_0/4$  and a weak system-reservoir coupling scale  $v = \omega_0/10$ . Unlike the other cases studied, this model has a current turnover profile that approaches the continuum limit  $I^\circ$  from below (Fig. S10). Such behavior precludes estimators for  $\gamma^*$  that minimize  $|I(\gamma) - I^\circ|/I^\circ$ , since the current maxima of the anomalies (both Markovian and virtual) approach  $I^\circ$  more rapidly than the interstitial, physical regime. We nonetheless find that the intersection estimator  $\gamma_s$  remains effective for identifying the physical regime of the plateau, exhibiting robust scaling for all quantities with respect to increasing  $N_W$  (Fig. S11). Within this context, the linear-inverse discretization continues to exhibit robust performance for all observables. Taken together, our observations underscore how our intersection estimator  $\gamma_s$  is generally robust when identifying optimal transport regimes — a fact that holds irrespective of plateau architecture or the manner in which the thermodynamic limit is approached.

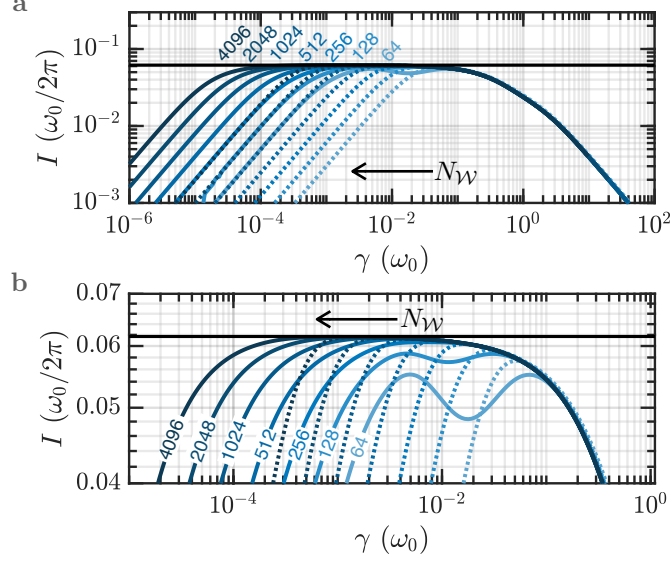


FIG. S10. **Kramers' turnover for a weakly coupled three-site impurity.** (a) Turnover in the steady-state current  $I$  for the non-interacting three-site model of Eq. (S2), taken at weak  $\mathcal{S}$ - $\mathcal{L}\mathcal{R}$  coupling ( $v = \omega_0/10$ ). The extended reservoirs have a linear discretization and the relaxation  $\gamma_k = \gamma$  is mode independent. Scaling is assessed with respect to the number  $N_W$  of explicit modes in each reservoir, for both on-resonant (solid) and off-resonant (dashed; with a level shift) configurations. (b) Inset of the data from (a) near the physical regime. The Landauer limit  $I^\circ$  for continuum reservoirs is shown by the solid, black horizontal line. Calculations are presented with on-site system frequencies  $\omega_j = 0 \cdot \omega_0$ , couplings of  $v_{12} = v_{23} = (1 + \sqrt{2})\omega_0/4$  between system sites, and strong system-reservoir coupling  $v = \omega_0/2$ . A bias of  $\mu = \omega_0/2$  is applied between  $\mathcal{L}$  and  $\mathcal{R}$  and a temperature  $k_B T = \omega_0/40$  is used for reservoir Fermi distributions. Couplings are provided by our integrated approach.

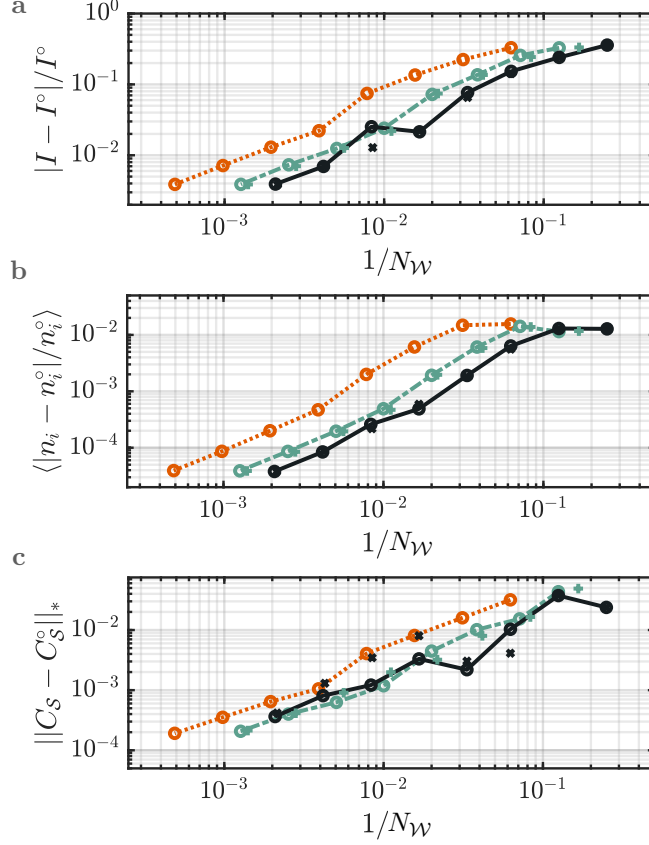


FIG. S11. **Estimator validation across discretizations for the weakly coupled three-site impurity.**

The intersection estimator  $\gamma_s$  is used to approximate the optimal relaxation regime  $\gamma^*$  in an analysis parallel to Fig. 6 of the primary manuscript. Convergence is shown for a weakly coupled ( $v = \omega_0/10$ ) three-site impurity (Eq. (S2) and Fig. S10) when increasing the number  $N_W$  of explicit reservoir modes. This behavior is quantified through (a) relative error in the steady-state current  $I$ ; (b) relative error in the on-site density  $n_i$  within  $\mathcal{S}$ ; and (c) the trace between the system correlation matrix  $C_S$  and its continuum reservoir counterpart  $C_S^o$ . The reference values ( $I^o$ ,  $n_i^o$  and  $C_S^o$ ) are taken in the continuum reservoir limit. Discretizations correspond to the standard linear (orange, dotted line), the linear-logarithmic (green, dashed line), and the linear-inverse (black solid line) arrangements. Results are also provided for additional linear-logarithmic and linear-inverse discretizations which are the transform of a 1D spatial lattice to the energy basis (green and black crosses). Parameters, methodology, and labels are otherwise identical to those of Fig. 6.

## ALTERNATIVE LINEAR–LOGARITHMIC DISCRETIZATIONS

### Method I

The logarithmic discretization from Eq. (4) and Fig. 6 is based on an influence scale that maintains continuity across the bias window edge. While convenient, continuity is not required. In fact, we can introduce a more general influence scale,

$$\chi_{\text{log-alt1}}(\omega) = \theta\left(\frac{\mu}{2} - |\omega|\right) + \frac{\alpha}{|\omega|}\theta\left(|\omega| - \frac{\mu}{2}\right), \quad (\text{S3})$$

that is specified by an independent discretization scale  $\Lambda = \omega_{k+1}/\omega_k$ . This is imposed by extending the bias window level spacing  $\Delta_0$  to the first logarithmic mode (e.g.,  $\Lambda = 1 + 2\Delta_0/\mu$ ). We then invoke the definition of our influence scale,

$$\int_{\mu/2}^{\mu/2+\Delta_0} \chi_{\text{log-alt1}}(\omega) d\omega = \Delta_0. \quad (\text{S4})$$

to establish a relationship  $\alpha = \frac{\Delta_0}{\log \Lambda}$  between these quantities. Unlike the approach of Eq. (4), this approach has two independent parameters and, thus, while it retains a linear and a logarithmic sector, it allows for them to be adjusted separately.

We find this alternate arrangement is comparable to the standard linear–logarithmic discretization for practical transport calculations (Fig. S12). When working at a discretization scale ( $\Lambda = 2.0$  to  $\Lambda = 3.0$ ) that is typical for the numerical renormalization group (NRG), we find only subtle variations in the calculated currents. While some deviations are seen at small  $N_{\mathcal{W}}$  for on–site densities and the system state, these vanish for a large number of reservoir sites.

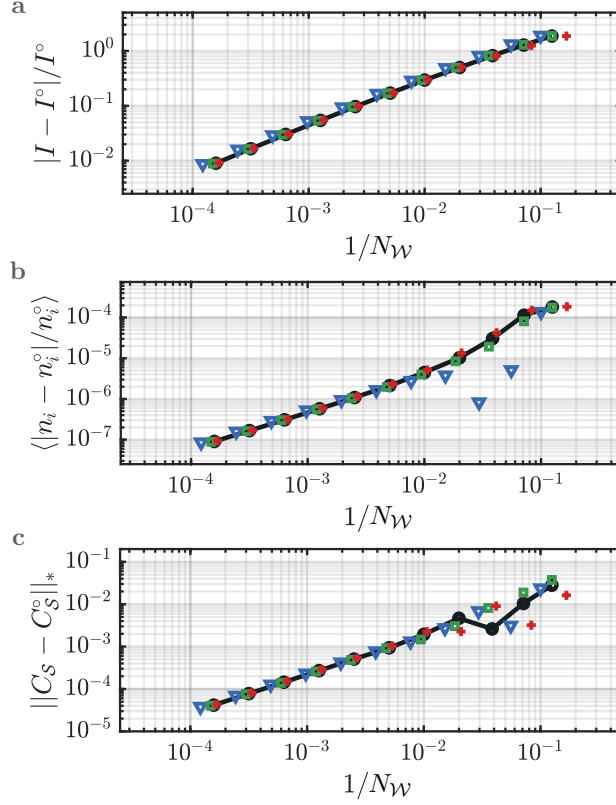


FIG. S12. **Error and discretization for an alternate linear–logarithmic discretization.** Convergence of the alternate linear–logarithmic discretization of Eq. (S4) at different discretization scales  $\Lambda$ . This behavior is quantified through (a) relative error in the steady–state current  $I[\gamma_k(\alpha^*)]$ ; (b) relative error in the on–site density  $n_i$  within  $\mathcal{S}$ ; and (c) the normalized trace distance between correlation matrix  $C_{\mathcal{S}}$  for  $\mathcal{S}$  and its infinite reservoir counterpart  $C_{\mathcal{S}}^o$ . Discretizations correspond to the standard linear–logarithmic influence of Eq. (4) of the primary manuscript (black solid line) and the alternate influence scale from Eq. (S4) with  $\Lambda = 2.0$  (blue triangles),  $\Lambda = 2.5$  (green squares), and  $\Lambda = 3.0$  (red crosses). All data are from the non–interacting, two–site Hamiltonian of Fig. 3b at weak–coupling ( $v_0 = \omega_0/10$ ), with integrated system–reservoir couplings, and relaxations  $\gamma = \alpha \langle \Delta_k \rangle_{\mathcal{B}}$  determined by the mean mode spacing within the bias window  $\mu = \omega_0/2$ .

## Method II

Here, we assess a third logarithmic discretization that has been used in prior many-body transport calculations (see Ref. [1]). We construct this by subdividing the reservoir bandwidth  $\mathcal{W}$  into bins of width  $\Delta_k = |\Omega_{k+1} - \Omega_k|$ , where the frequencies  $\Omega_k$  are indexed by  $k \in \mathbb{Z}$ . The sign of  $k$  corresponds to the sign of the associated frequency. We then arrange the  $\Omega_k$  to give  $N_\mu = \mu/\Delta_0$  linearly spaced bins inside the bias window. Modes far outside the bias window will be distributed logarithmically (e.g.,  $\Omega_{k+1}/\Omega_k = \Lambda$  for  $k > 0$ ) with  $\Lambda$  setting the logarithmic discretization scale. As with Method I, this permits independent adjustment of the linear and logarithmic sectors. The full distribution of  $\Omega_k$  is then defined to interpolate between these limits,

$$\Omega_k = \begin{cases} \Delta_0 \cdot k, & \text{if } |k| \leq N_\mu/2, \\ \Delta_0 \cdot \left( \frac{\sinh\left[\left(k \mp \frac{N_\mu}{2}\right) \log \Lambda\right]}{\log \Lambda} \pm \frac{N_\mu}{2} \right) & \text{if } |k| > N_\mu/2. \end{cases} \quad (\text{S5})$$

This set is used to specify mode placement, assuming that the extremal bins bounded by the band edges at  $\pm\mathcal{W}/2$ . We take two approaches to define the modes  $\omega_k$ . In the first, we place modes at the midpoint of each bin so that  $\omega_k = [\Omega_{k+1} + \Omega_k]/2$ . The second follows Ref. [1], where we set

$$\omega_k = \begin{cases} \frac{\Omega_{k+1} - \Omega_k}{\log(\Omega_{k+1}/\Omega_k)} & \text{if } |\Omega_k|, |\Omega_{k+1}| > \mu/2, \\ \frac{1}{2}[\Omega_{k+1} + \Omega_k] & \text{otherwise.} \end{cases} \quad (\text{S6})$$

We introduce couplings  $v_{jk}$  that reproduce the integrated weight within each bin and relaxations  $\gamma_k$  that are specified by the mode spacing in the bias window (as used in Fig. 6).

In practice, the discretization specified by Eq. (S5) is insensitive to how modes are placed within a given frequency bin (Figs. S13 and S14, respectively). Furthermore, it scales more efficiently for currents than the standard linear-logarithmic method from Eq. (4), provided that  $N_{\mathcal{W}}$  is small. This is not surprising, as transport is dominated by states in the bias window and the method of Eq. (S5) favors this region. Nonetheless, the observed benefit saturates beyond the number of modes typical for most many-body simulations ( $N_{\mathcal{W}} \approx 128$ ), while the saturation point has a moderate dependence on the discretization scale  $\Lambda$ . Such behavior is also expected, as the bandwidth outside the bias window is heavily coarse-grained and relevant correlations may be missed. This is also reflected through a saturation in on-site densities and without a well-defined trend for the error in the system state.

This behavior is not unexpected for a two parameter family. The lin-log discretization of the main text links  $\Delta_0$  and  $\Lambda$ , taking the continuum limit of both together. Method I and II, however, have independent adjustment of these two parameters. When they are not balanced, this can cause a saturation in error as further decrease of one parameter (towards the continuum limit) can not capture what is missing due to the fixed value of the other parameter.

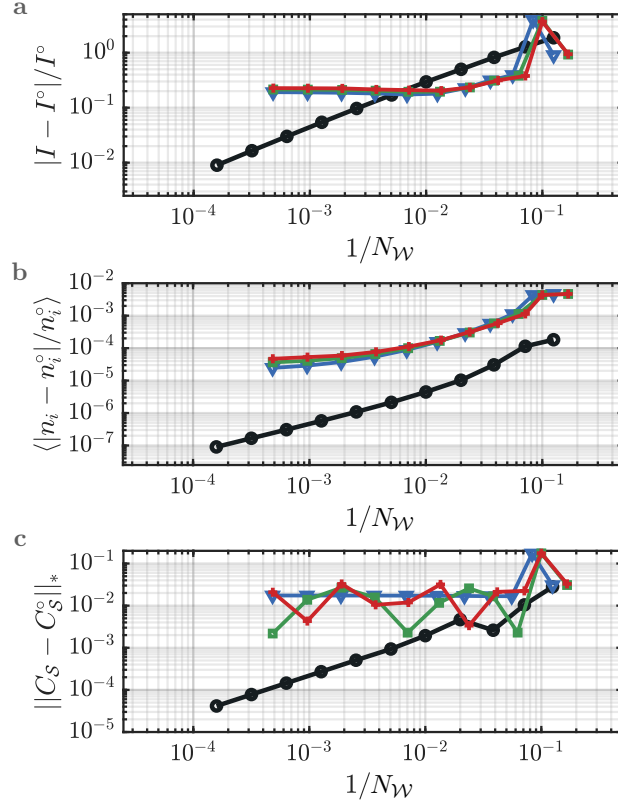


FIG. S13. **Error and discretization for an alternate (Method I) linear–logarithmic discretization.**

Convergence of the alternate linear–logarithmic discretization of Eq. (S5) at different discretization scales  $\Lambda$ . Here, the reservoir modes are defined by placing them at the center of each discretization bin. This behavior is quantified through (a) relative error in the steady–state current  $I[\gamma_k(\alpha^*)]$ ; (b) relative error in the mean on–site density  $n_i$  within  $\mathcal{S}$ ; and (c) the normalized trace distance between correlation matrix  $C_{\mathcal{S}}$  for  $\mathcal{S}$  and its infinite reservoir counterpart  $C_{\mathcal{S}}^{\circ}$ . Discretizations correspond to the standard linear–logarithmic influence scale of Eq. (4) of the primary manuscript (black circles) and the alternate influence scale from Eq. (S5) with  $\Lambda = 2.0$  (blue triangles),  $\Lambda = 2.5$  (green squares), and  $\Lambda = 3.0$  (red crosses). All data are from the non–interacting, two–site Hamiltonian of Fig. 3b at weak–coupling ( $v_0 = \omega_0/10$ ), with integrated system–reservoir couplings, and relaxations  $\gamma = \alpha \langle \Delta_k \rangle_{\mathcal{B}}$  determined by the mean mode spacing within the bias window  $\mu = \omega_0/2$ .

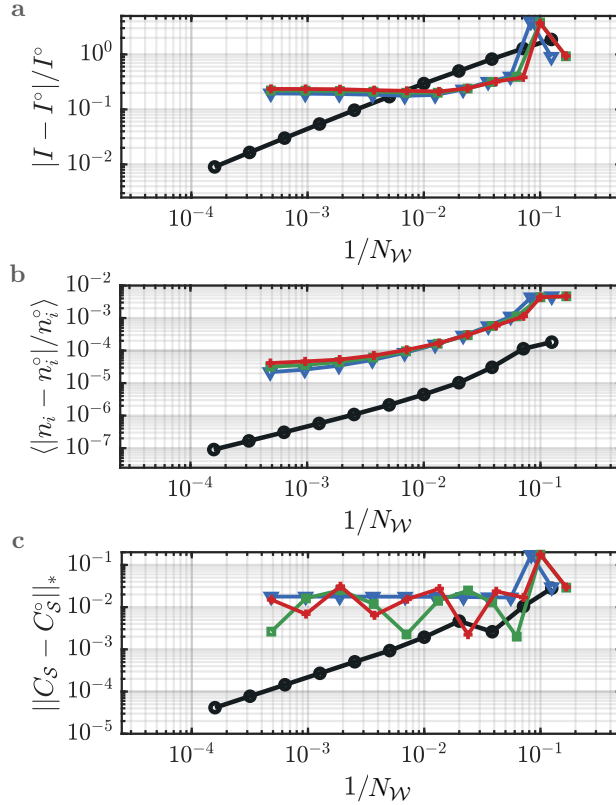


FIG. S14. **Error and discretization for an alternate (Method II) linear-logarithmic discretization.** Convergence of the alternate linear-logarithmic discretization of Eq. (S5) at different discretization scales  $\Lambda$ . Here, the reservoir modes are defined according to Eq. (S6). This behavior is quantified through (a) relative error in the steady-state current  $I[\gamma_k(\alpha^*)]$ ; (b) relative error in the mean on-site density  $n_i$  within  $\mathcal{S}$ ; and (c) the normalized trace distance between correlation matrix  $C_{\mathcal{S}}$  for  $\mathcal{S}$  and its infinite reservoir counterpart  $C_{\mathcal{S}}^{\circ}$ . Discretizations correspond to the standard linear-logarithmic influence scale of Eq. (4) of the primary manuscript (black circles) and the alternate influence scale from Eq. (S5) with  $\Lambda = 2.0$  (blue triangles),  $\Lambda = 2.5$  (green, squares), and  $\Lambda = 3.0$  (red, crosses). All data are from the non-interacting, two-site Hamiltonian of Fig. 3b at weak-coupling ( $v_0 = \omega_0/10$ ), with integrated system-reservoir couplings, and relaxations  $\gamma = \alpha \langle \Delta_k \rangle_{\mathcal{B}}$  determined by the mean mode spacing within the bias window  $\mu = \omega_0/2$ .

---

\* marek.rams@uj.edu.pl

† mpz@nist.gov

[1] F. Schwarz, I. Weymann, J. von Delft, and A. Weichselbaum, Phys. Rev. Lett. **121**, 137702 (2018).